Article:
Williams, Sophie, Garrett, Ed, Moss, Patrick et al. (7 more authors) (2023) Relative sea-level changes in southeastern Australia during the 19th and 20th centuries. Journal of Quaternary Science. ISSN: 0267-8179

https://doi.org/10.1002/jqs.3528

JOURNAL OF QUATERNARY SCIENCE (2023) 1–18 ISSN 0267-8179. DOI: 10.1002/jqs.3528

JQS Journal of Quaternary Science QRA Quaternary Research Association

Relative sea-level changes in southeastern Australia during the 19th and 20th centuries

S. L. WILLIAMS,[1,2]* E. GARRETT,[2] P. T. MOSS,[3] S. DANGENDORF,[4] F. D. HIBBERT,[2] N. R. ATKINSON,[5] V. PASHLEY,[5] I. L. MILLAR,[5] M. H. GARNETT,[6] A. ZAWADZKI[7] and W. R. GEHRELS[2]

[1]Department of Geography, Durham University, Durham, UK
[2]Department of Environment and Geography, University of York, York, UK
[3]School of Earth and Environmental Sciences, The University of Queensland, Brisbane, Australia
[4]Department of River-Coastal Science and Engineering, Tulane University, New Orleans, LA, USA
[5]British Geological Survey, Nicker Hill, Keyworth, Nottingham, UK
[6]NEIF Radiocarbon (Environment), SUERC, East Kilbride, UK
[7]Australian Nuclear Science and Technology Organisation (ANSTO), NSW, Australia

Received 30 August 2022; Revised 31 March 2023; Accepted 8 April 2023

ABSTRACT: Rates of global and regional sea-level rise between ~1850 and 1950 were high compared to those in preceding centuries. The cause of this sea-level acceleration remains uncertain, but it appears to be pronounced in a small set of relative sea-level proxy records from the Southern Hemisphere. Here we generate three new proxy-based relative sea-level reconstructions for southeastern Australia to investigate spatial patterns and causes of historical sea-level changes in the Tasman Sea. Palaeo sea-level estimates were determined using salt-marsh foraminifera as sea-level indicators. Records are underpinned by chronologies based on accelerator mass spectrometry ^{14}C, radiogenic lead (^{210}Pb), stable lead isotopes and palynological analyses. Our reconstructions show that relative sea level rose by ~0.2–0.3 m over the last 200 years in southeastern Australia, and rates of sea-level rise were especially high over the first half of the 20th century. Based on modelled estimates of the contributing components to sea-level rise, we suggest that the episode of rapid sea-level rise was driven by barystatic contributions, but sterodynamic contributions were dominant by the mid-20th century. Significant spatial variability in relative sea level indicates that local to sub-regional drivers of sea level are also prominent. Our reconstructions significantly enhance our understanding of the spatiotemporal pattern of early 20th century sea-level rise in the region.

KEYWORDS: Australia; Gaussian process; microfossil; salt marsh; sea level

Introduction

Future sea-level rise as a consequence of global warming is projected to be one of the main threats to civilization, affecting hundreds of millions of people living in coastal regions across the globe (Dangendorf et al., 2019; Oppenheimer et al., 2019). Current estimates of global mean sea-level rise (1900–2018) indicate a trend of 1.6 ± 0.3 mm a^{-1} (Church & White, 2006; Dangendorf et al., 2019; Frederikse et al., 2020; Hay et al., 2015; Palmer et al., 2021). Rates of at least 2.9–6.1 mm a^{-1} are predicted for 2040–2060, which may increase to 2.5–6.6 mm a^{-1} between 2080 and 2100 under even the lowest emissions scenario (Fox-Kemper et al., 2021). Quantifying past sea-level change using geological proxy records can contextualize current and future rates of sea-level rise and ascertain the relative contributions of natural and anthropogenic processes that are the underlying causes of historical global and regional sea-level change (Jevrejeva et al., 2010; Kopp et al., 2016). This is important when considering whether current rates of sea-level change are unprecedented, and what this may then mean for future adaptation and mitigation strategies.

High-resolution geological proxy records of Holocene and Common Era relative sea-level (RSL) changes from across the globe have mostly been derived from salt-marsh sediments (e.g. Long et al., 2010, 2014; Saher et al., 2015; Kemp *et al.*, 2017a; Barnett et al., 2019; Gehrels et al., 2020). They demonstrate that rates of sea-level rise have deviated considerably from the late Holocene background rate, with many showing a sea-level acceleration between ~1850 and 1950 (e.g. Gehrels et al., 2005; Gehrels et al., 2008; Gehrels et al., 2012; Kopp et al., 2015; Gerlach et al., 2017; Kemp et al., 2017b; Barnett et al., 2019). This acceleration occurred largely before anthropogenic forcing became dominant (Slangen et al., 2016). Temporal evolution of the natural and anthropogenically forced contributions to sea level, and thus changes in the magnitudes and rates of sea-level change over the Common Era, can be assessed by undertaking a global analysis. This is done by employing a spatiotemporal empirical hierarchical model that characterizes RSL in both space and time (e.g. Kopp et al., 2016; Walker et al., 2021). At a process level, RSL is modelled as a function of several terms including: globally uniform terms, a regional linear term, regional non-linear terms and local non-linear terms (Walker et al., 2021). Hyperparameters are used to define priors such as timescales of RSL variability (i.e. centennial, millennial). Reconstructions of RSL, including vertical and age uncertainty, can then be compared to the RSL process and the reconstructions decomposed into the various terms. When a global database of RSL proxy data is included in the model, rates of global sea-level

*Correspondence: S. L.Williams, as above.
E-mail: sophie.williams@durham.ac.uk

change can be inferred (Kopp et al., 2016; Walker et al., 2021). However, these compilations are spatially biased, with few high-resolution sea-level reconstructions from the Southern Hemisphere in comparison to the Northern Hemisphere (particularly the North Atlantic; Walker et al., 2021).

The few available proxy sea-level records from Australia and New Zealand document a rise in sea level ~1 mm a^{-1} greater on average compared to records from the North Atlantic region over the first half of the 20th century (Gehrels et al., 2012, 2020; Gehrels & Woodworth, 2013; Kopp et al., 2016; Garrett et al., 2022), which could point to a far-field (i.e. Northern Hemisphere) melt source due to the effects of gravity, rotation and deformation (GRD; e.g. Bamber & Riva, 2010; Frederikse et al., 2020). A possible explanation may be melting of land-based ice masses that retreated from their 19th century maxima at the end of the Little Ice Age (Marzeion et al., 2014). Indeed, early 20th century global mean sea-level rise was largely driven by the melting of glaciers and, to a lesser extent, ice sheets (e.g. Parkes & Marzeion, 2018; Frederikse et al., 2020; Malles & Marzeion, 2021). However, the acceleration is not temporally consistent across RSL records, which may indicate other regional and local-scale sea-level processes acting in combination with the barystatic component to drive sea-level changes. For example, recent findings from New Zealand (Garrett et al., 2022) suggest a dominant role of sterodynamics (i.e. the combination of steric expansion and changes in ocean circulation) in driving fast rates of sea-level rise over the early to mid-20th century. However, it remains difficult to definitively ascertain the causes behind the acceleration in the Australian and New Zealand records due to the limited network of long-term observational data and proxy records. In the North Atlantic, spatiotemporal hierarchical models have been used to extract the local and regional non-linear signals to better understand the drivers of Common Era sea-level change (Walker et al., 2022), but this is not yet possible for the Southern Hemisphere.

In this study, we create three new proxy-based RSL reconstructions for southeastern Australia to supplement sparse tide-gauge data, which increases the number of records from the region that can be used in regional and global analyses (cf. Kopp et al., 2016; Walker et al., 2021). We contextualize current and future rates of sea-level rise in the region by assessing sea-level variability over the past two centuries, and verify the existence, magnitude and timing of periods of rapid sea-level rise, as well as investigate driving mechanisms.

Study sites

Salt marshes are useful sedimentary archives of sea-level change as they accrete vertically in fine layers in response to sea-level rise (e.g. Gehrels et al., 2005, 2006, 2020; Kemp et al., 2011, 2017a). Microfossil and chronological analyses of such archives yield high-resolution sea-level reconstructions (Barlow et al., 2013). We sampled three salt marshes in southeastern Australia, one each in Tasmania (Lutregala), New South Wales (Wapengo) and Victoria (Tarra) (Fig. 1).

Lutregala

Lutregala (Indigenous name lunawanna-allonnah; 43.299°S, 147.307°E) is located on South Bruny Island in southeastern Tasmania, ca. 70 km south of the city of Hobart. The marsh is ~0.4 km^2 in size and fronts onto Simpsons Bay (Prahalad & Jones, 2013). Williams et al. (2021) modelled a tidal range of 0.91 m at the site. Mean salinity is 32.8 ppt (Crawford & Mitchell, 1999). The marsh is dominated by salt-loving plants *Juncus krausii* (salt-marsh rush), *Gahnia filum* (chaffy saw sedge), *Sarcocornia quinqueflora* (beaded glasswort), *Tecticornia arbuscula* (shrubby glasswort), *Samolus repens* (sea primrose) and *Suaeda australis* (seablite). Whilst permanent European settlement of North Bruny commenced in ~1818 CE (Nethery, 2012) official settlement of South Bruny Island was not recognized until the 1850s to 1870s, when coal mining and the timber industry grew in importance.

Wapengo

Wapengo Marsh is located ~30 km south of Bermagui in southern New South Wales (Fig. 1). The salt marsh is ~0.51 km^2 in extent (Creese et al., 2009) and is located at the northern end of the Wapengo Lake estuary, which features a narrow bedrock-framed mouth called Bithry Inlet. Salinity in the estuary is ~34–37 ppt (Garside et al., 2014) and the modelled mean tidal range is 0.95 m (Williams et al., 2021). The marsh is dominated by *J. kraussii, G. filum* and *S. quinqueflora* as well as a lower abundance of *T. arbuscula* and *Distichlis distichophylla* (Australian salt grass). At the seaward end *Avicennia marina* (grey mangrove) encroaches into the marsh; this develops into a dense mangrove forest at lower elevations. European settlement of the area around Wapengo occurred ~1830–1840 CE (Lunney & Leary, 1988); however, an intensification of land use did not occur until 1861 CE, with the introduction of grazing and non-native plant and tree species into the area, reaching a peak towards the end of the 19th century and early 20th century (Lunney & Leary, 1988).

Tarra

Tarra is located along the Nooramunga coast in East Gippsland, Victoria, ~4 km from Port Albert (Fig. 1). The salt marsh is ~1.7 km up the Tarra River and ~1.37 km^2 in extent. This part of the Victoria coast is characterized by extensive sand and mud flats, tidal channels and sandy barrier islands known as the Nooramunga Islands. Tidal modelling following the approach used in Williams et al. (2021) predicts a tidal range of 1.25 m. A narrow fringe of *Melaleuca* is present around the marsh, which is dominated by *D. distichophylla, S. repens, S. quinqueflora, J. krausii* and *T. arbuscula*. *Distichlis distichophylla* and *S. quinqueflora* are most dominant at higher marsh elevations and *J. krausii*, *S. australias* and *T. arbuscula* increase at lower elevations. Similarly to Wapengo, the marsh is fronted by *A. marina*. Following European settlement of the area in 1841 CE, the population of the area expanded rapidly during the early 1840s and 1850s.

Methods

Field methods

We conducted an initial stratigraphic inspection along coring transects at each site with a hand-held gouge corer (0.5 × 0.03 m) to ascertain the area of the marsh with the thickest salt-marsh peat that might provide the longest sea-level record (Fig. 1). We took master cores from each site using either a wide-diameter gouge (0.5 × 0.06 m) or Russian peat sampler (0.5 × 0.06 m). All cores were surveyed relative to a temporary local survey peg using a Trimble M1 (DR2″) total station and linked to Australian Height Datum (AHD) 2020 using a Trimble R4 real-time kinematic GNSS. We analysed fossil foraminifera in each master core at 1-cm resolution. Species were picked, identified and counted using the methods described by Williams et al. (2021).

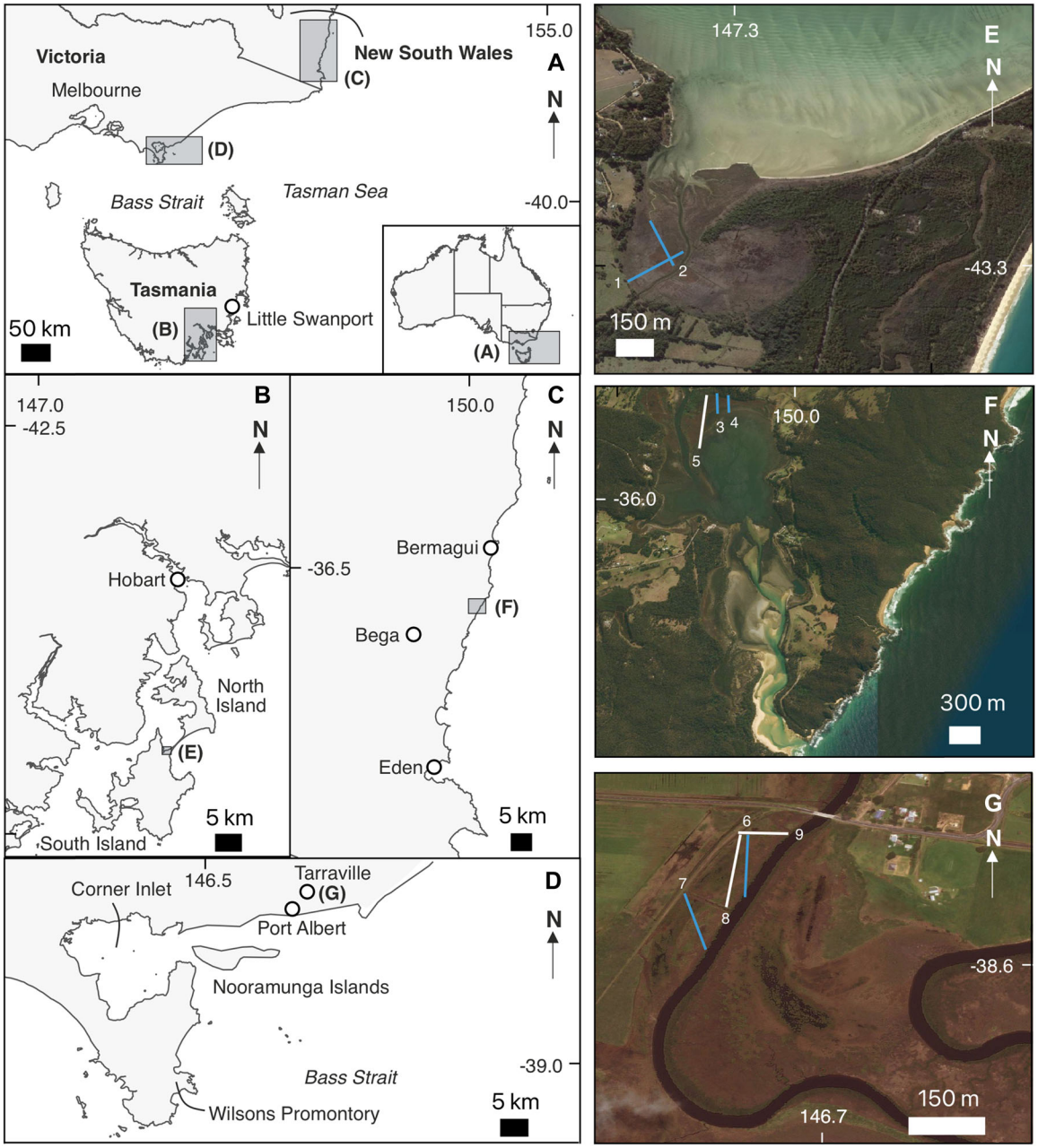

Figure 1. Map of the study sites showing A, regional-scale overview; B, sub-regional overview of the Lutregala study area on South Bruny Island; C, sub-regional overview of the Wapengo study area; D, sub-regional overview of the Tarra study area; E, Lutregala salt marsh; F, Wapengo salt marsh; and G, Tarra salt marsh. White numbers correspond to transect numbers in Fig. 3. Blue transects were used as both surface and coring transects (Williams *et al.*, 2021) and white transects were used only as coring transects (this study). Basemaps in E, F and G are from Google Earth. [Color figure can be viewed at wileyonlinelibrary.com]

Transfer functions and palaeomarsh surface elevation reconstruction

For Lutregala and Wapengo, we used weighted-averaging partial least squares sea-level transfer functions previously developed by Williams et al. (2021) to generate palaeomarsh surface elevation (PMSE) estimates for fossil samples in our master cores (see 'Transfer functions' in the Results). For Tarra, we counted foraminifera in 41 surface samples and developed a new local transfer function following the methodology described by Williams et al. (2021). We quantified PMSEs for samples with total foraminiferal counts >50 individuals (following Kemp et al., 2020) using the R package '*rioja*' (Juggins, 2020). To convert PMSE estimates into RSL estimates, we took the field elevation of each sample and subtracted the PMSE estimate. To assess the reliability of resulting PMSE estimates we compared the fossil assemblages with modern ones by employing the Modern Analogue Technique in *rioja*. We use the 'Square Chord' dissimilarity metric (Birks, 1995) as this method is optimal for count data such as those used in this study and helps to minimize the signal to noise ratio (Kemp & Telford, 2015). We define the threshold between good, fair and poor modern analogues using the dissimilarity between the samples in the modern training set. In line with recommendations from Kemp and Telford (2015), we choose the 20th percentile as the threshold for analogy as the diversity of the modern training sets are low. Following Watcham et al. (2013), we define 'good' analogues as samples with minimum dissimilarity values below the 5th percentile and 'fair' analogues as those with values between the 5th and 20th percentiles. For further details on the derivation of the transfer functions, refer to Williams et al. (2021).

Establishing chronologies

Dating of recent salt-marsh sediment can be problematic due to both the radiocarbon 'plateau' in the last 300 years, as well as the limited span (~100–150 years) of ^{210}Pb (Kemp et al., 2012). Therefore, to obtain a high-resolution chronology, we employed a range of dating techniques which included radiocarbon (^{14}C) dating by accelerator mass spectrometry (AMS), as well as ^{210}Pb, stable lead isotope ratios and pollen (cf. Gehrels et al., 2008, 2012; Kemp et al., 2012). Samples for ^{14}C were analysed at the Scottish Universities Environmental Research Centre (SUERC), the University of California, Irvine (UCI) and the Australian Nuclear Science and Technology Organisation (ANSTO). We use bomb-spike AMS ^{14}C for sediments younger than ~60 years old and high-precision (multiple target) AMS ^{14}C (Marshall et al., 2007) or routine precision for sediments older than ~60 years old. We targeted horizontally bedded above-ground parts of terrestrial plants, but dated bulk sediment in several instances where insufficient macrofossils were encountered. Full details of the preparation methodology are given in supplementary file 1 (see Supporting Information S1). We calibrated pre-bomb spike ^{14}C dates using the SHCal20 calibration curve (Hogg et al., 2020) and calibrated post-bomb spike dates using the Bomb13 SH1–2 calibration curve (Hua et al., 2013) in '*rplum*' (Aquino-López et al., 2020; Blaauw, 2021).

Preparation and analyses of the ^{210}Pb samples were undertaken at ANSTO by alpha particle spectrometry. Samples were processed for the determination of total ^{210}Pb, measured indirectly from its progeny polonium-210 (^{210}Po) and supported ^{210}Pb, measured from its grandparent radioisotope radium-226 (^{226}Ra). Unsupported ^{210}Pb activity was estimated by subtracting supported ^{210}Pb from the total ^{210}Pb activity.

Stable Pb isotope analyses were undertaken at the Geochronology and Tracers Facility at the British Geological Survey using a Nu Instruments, Nu Plasma HR, MC-ICP-MS (multi-collector-inductively coupled plasma-mass spectrometer). Sediment samples were taken at contiguous 1-cm intervals and prepared for isotope analysis (for the full preparation and mass spectrometry analysis methodology see S2 in Supporting Information 1).

Pollen and microcharcoal analyses were conducted at the University of Queensland to provide additional chronohorizons. Pollen preparation methods followed those outlined in Moss et al. (2013) and macrocharcoal preparation followed guidelines in Stevenson and Haberle (2005).

We generated Bayesian age–depth models in *rplum* to combine chronological information from the different methods and interpolate the age of every foraminiferal sample. As with traditional constant rate of supply models (e.g. Appleby & Oldfield, 1978), *rplum* assumes a constant rate of supply of ^{210}Pb; however, it separates the age–depth modelling process from the ^{210}Pb decay equation by using a self-adjusting Markov chain Monte Carlo (MCMC) algorithm (Sim et al., 2021). Calendar dates identified from chronohorizons in the core using the stable lead profile and pollen and charcoal records were assigned a date and uncertainty based on archival dates from the literature.

Reconstructing sea level

Following Gehrels et al. (2020), we used (error-in-variable) Gaussian process regression, accounting for both temporal and vertical uncertainties, to model sea-level change at Lutregala, Wapengo and Tarra. The temporal covariance (defining the variance of its mean and temporal correlations) was represented by a Matérn function with a smoothness factor of 3/2. All corresponding hyperparameters (length scale for the definition of the temporal correlation between different points in time, and scale for the description of variability of the process) were estimated using an automatic hyperparameter optimization algorithm implemented in MATLAB's '*fitrgp*' function. Both chronological and vertical uncertainties were assumed to be normally distributed. A Monte Carlo approach using 5000 iterations was used to estimate sea-level change at each site over time. Individual sea-level index points were glacio-isostatic adjustment (GIA) corrected using estimates from the Caron et al. (2018) model assuming that GIA is a linear process over the time periods considered here (~200 years). This model considers uncertainties by varying the rheology and ice history in each realization, and a representative set of 5000 GIA model iterations was used to obtain RSL estimates at each site (the 5000 estimates define the total size of the Monte Carlo experiment). As a result, 5000 different RSL reconstructions are derived from which median values and 95% confidence limits (2.5 and 97.5th percentiles) were extracted. Compaction is considered negligible in the thin salt-marsh sediments from the region (Brain et al., 2012; Gehrels et al., 2012).

The selection of tide-gauge stations was based both on the geographical distance to the proxy sites and temporal coverage. Tide-gauge data were taken from Hogarth (2014) and GIA-corrected. Stations in close proximity to the marshes are limited to the last ~30 years. Long-term tide-gauge stations are located hundreds of kilometres from the sites and, in the case of Port Arthur, contain significant data gaps in the record (Fig. 2).

In the absence of long tide-gauge records in close vicinity to the marshes we follow Garrett et al. (2022) to calculate localized sea-level budgets (i.e. modelled estimates of the contributing components to sea-level rise) for each site. We use sterodynamic estimates from the SODAsi.3 ocean re-analysis model (Giese et al., 2016), present-day barystatic (including GRD) estimates from Frederikse et al. (2020) and the inverse barometer effect calculated from sea-level pressure fields from the 20th century re-analysis project v3 (Slivinski et al., 2019). GIA was not considered in the budgets as we compared them to GIA-corrected proxy and tide-gauge records. We do not consider any inherent uncertainties in the individual budget components, as they are only available for the present-day barystatic components, but not for the ocean reanalyses and the inverse barometer effect.

As proxy records filter interannual variability (i.e. several years up to several decades can be recorded in a single centimetre of a core depending on the sedimentation rate), tide-gauge records and budgets were 30-year smoothed. For the local tide-gauge data and budgets, this was done using a Singular Spectrum Analysis (Moore et al., 2005) with an embedding function of 15. For the long-term tide-gauge records, this was done using a Gaussian-weighted moving average filter as the records contain some significant data gaps and so Singular Spectrum Analysis could not be used.

Results

Transfer functions

Transfer functions developed by Williams et al. (2021) were used to generate PMSE estimates at Lutregala and Wapengo (Table 1). For Tarra, a screened local training set (36 samples) of foraminifera was generated from the two transects, which, when combined, have a vertical range of 0.6 m (see Supporting Information Fig. S3.1). Species encountered are

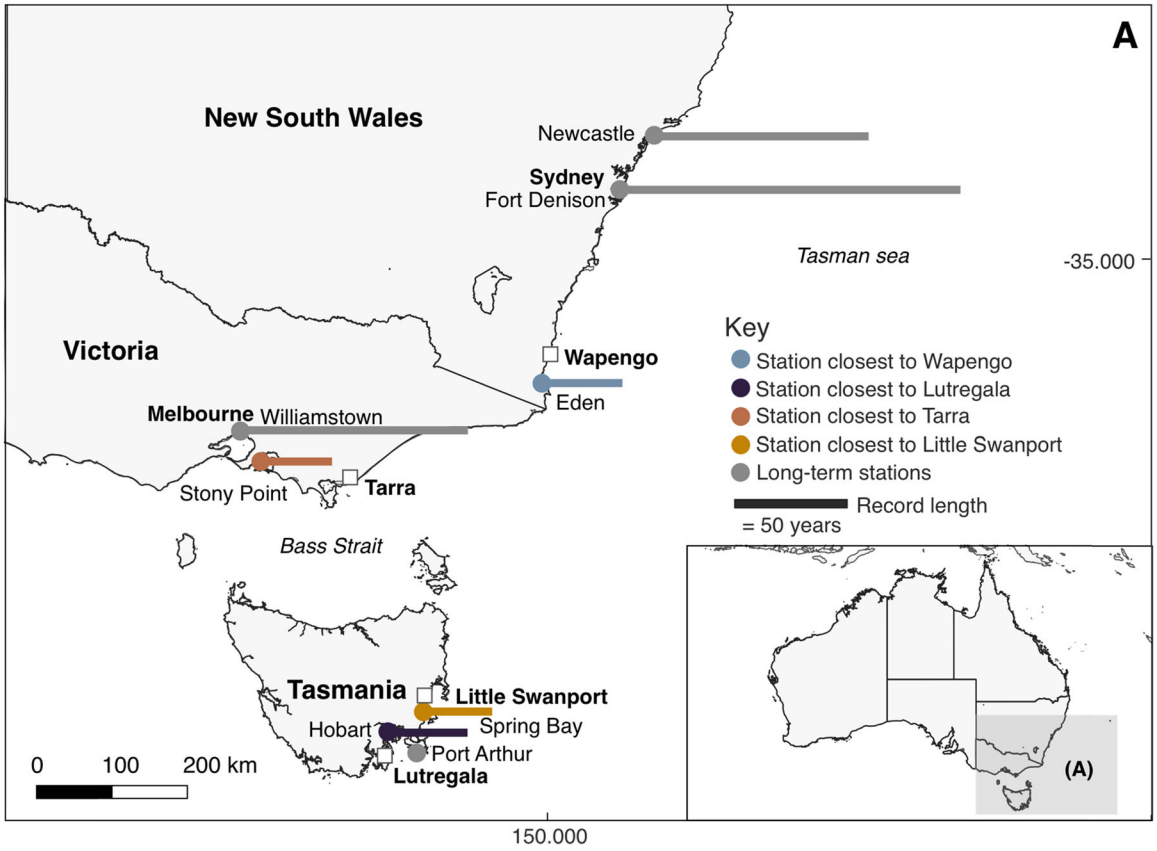

Figure 2. Locations of the tide gauges closest to each site (coloured dots) and locations of long-term tide gauges (grey dots). Horizontal bars are scaled to the length of the tide-gauge record in years – an example is given in the key. The Port Arthur tide gauge location is shown, but the record length is not plotted owing to significant data gaps in the record. Marshes at Wapengo, Lutregala and Tarra (this study) and Little Swanport (Gehrels *et al.*, 2012) are represented by white squares. [Color figure can be viewed at wileyonlinelibrary.com]

similar to those at Lutregala & Wapengo (Williams et al., 2021) including: *Trochamminita salsa, Haplophragmoides wilberti, Polysacammina ipohalina, Trochammina irregularis, Entzia macrescens, Trochammina inflata, Siphotrochammina lobata, Miliammina fusca* and *Ammobaculites exiguus*, as well as *Ammotium fragile* (not previously encountered at either site). There is little vertical zonation of foraminifera and *T. inflata* dominates across the majority of the vertical gradient (average 65% abundance, maximum 97% abundance). Detrended canonical correspondence analysis indicates a linear response of the foraminifera to elevation, and therefore a partial least squares regression model (Wold et al., 1984) was used. The resulting transfer function performed very poorly in terms of the relationship between observed and predicted elevations (root mean squared error of prediction: −0.08 m; r^2_{boot}: 0.02; see Fig. S3.2). Many of the samples were predicted at the same height, ~1.20–1.25 m (Fig. S3.2). We suggest this is due to the dominance of *T. inflata* across the marsh. As species optima are similar between foraminifera in the local and regional training sets (Fig. S3.3) there are several options: (i) use the existing southeastern Australia regional II training set for the Tarra reconstruction; (ii) include the Tarra samples in a regional training set with existing samples; or (iii) follow, for example, Long et al. (2014) and assign conservative semi-quantitative indicative ranges based on stratigraphy and common species. When samples are incorporated into the existing southeastern Australia regional transfer function (Williams et al., 2021), the model r^2_{boot} reduces from 0.69 to 0.54 and maximum and average bias increases as many of the samples, like in the local transfer function, are predicted at the same elevation. Furthermore, the Tarra surface samples do not provide a wider range of analogues than the existing regional training set; therefore, we do not include them. The present-day salt marsh extends between 1.35 and 1.01 m AHD, which yields an indicative range for salt-marsh sediments of 1.18 ± 0.17 m. We cannot assign a narrower vertical range based on comparing the fossil and local modern foraminiferal assemblages, as foraminifera found at both the upper and lower elevation limits in the modern environment at Tarra are present in the core. Using the regional II training set to estimate PMSE results in ranges of 1.12 ± 0.12 to 1.33 ± 0.12 m AHD, with an average of 1.20 ± 0.12 m AHD. Therefore, both approaches result in very similar outputs. Finally, we also compared the poorly performing local transfer function PMSE estimates with the regional PMSE estimates. The PMSE estimates of both models overlap significantly, further suggesting that the regional model is appropriate.

Lutregala stratigraphy and foraminiferal assemblages

We established two coring transects at Lutregala which followed the surface sampling transects (Williams et al., 2021; Fig. 1). At the base of the sequence at Lutregala (Unit 3; Fig. 3a) is a silty sand unit which extends down to at least −1.24 m AHD. Overlying this unit is a silt (Unit 2) which was thickest towards the seaward and landward sides of the salt marsh. At the surface of the sequence is a salt-marsh peat (Unit 1). The maximum peat thickness is 28 cm. Unit 1 was subdivided into a silty salt-marsh peat at the bottom (1b), and a fibrous salt-marsh peat at the top (1a).

The foraminiferal assemblages in the silty sand unit mainly consist of the high to mid-marsh species *T. inflata* (average relative abundance 96%), with a low abundance of *T. salsa*

Table 1. Summary of transfer function performance statistics.

Training set	Scale	Sites included in the model	Number of samples	Number of species	Model type and component number	RMSEP (SWLI)	RMSEP (m AHD)	r^2_{boot}	Average bias (SWLI)	Maximum bias (SWLI)
Lutregala	Local	Lutregala	37	9	WAPLS C1	6.42	0.06	0.65	–0.01	7.86
Wapengo	Local	Wapengo	29	12	WAPLS C1	9.73	0.11	0.56	0.12	20.32
Tarra	Local	Tarra	36	10	PLS C1	4.83	0.08	0.02	0.17	–2.77
Little Swanport	Local	Little Swanport	41	6	PLS C1	15.23	0.11	0.42	0.11	32.74
Sub-regional	Sub-regional	Lutregala & Little Swanport	76	9	PLS C1	12.64	–	0.41	0.00	32.83
Regional I	Regional	Lutregala, Wapengo & Little Swanport	105	13	PLS C1	12.91	–	0.34	0.06	35.12
Regional II	Regional	Lutregala & Wapengo	65	13	WAPLS C1	7.66	–	0.69	0.07	9.15
Regional III	Regional	Lutregala, Wapego & Tarra	103	14	WAPLS C1	7.87	–	0.54	0.93	13.68

RMSEP, root mean squared error of prediction; AHD, Australian Height Datum; SWLI, standardized water level index.

and *E. macrescens.* Total counts are low in the unit (average of 19 specimens per sample). Foraminifera in the silt unit largely comprise *T. inflata* (average 96% relative abundance) and average total counts are higher (average of 56 individuals per sample). Within the silty salt-marsh peat, unit 1b, *T. salsa* is more prevalent (average 39%, up to a maximum of 75% relative abundance). Into the fibrous salt-marsh peat, unit 1a, the relative abundance of *T. salsa* declines and the assemblages diversify, with *T. inflata*, *E. macrescens* and *M. fusca* increasing. Total counts are largest in this unit (average 219 individuals per sample).

Modern analogue results (Table 2) show that all samples have at least fair modern analogues in the regional or local Lutregala training sets, suggesting that fossil assemblages are mostly similar to modern assemblages. The larger number of fair rather than good analogues in the lower third of the core (Fig. 4a) is due to the relative abundances of *T. inflata* being higher in the core than in the modern surface samples (Williams et al., 2021). Whilst the regional model results in a larger number of good modern analogues compared to the local model, there is very little difference in PMSE estimates between the two models (Fig. 4a) and, owing to the reduced vertical error of the local model compared to the regional model, we choose to employ the local transfer function.

Only one sample from the silty sand unit contained more than 50 specimens; the resulting PMSE reconstruction indicates the sample accumulated at around 0.71 m AHD, an elevation corresponding to the modern mid- to high marsh. PMSE predictions in this silt show that the marsh elevation remained largely unchanged from the silty sand, and foraminifera remain indicative of a mid- to high salt-marsh environment. In the silty salt-marsh peat, corresponding with the increase in *T. salsa*, PMSE increased by 0.21 ± 0.08 m, reaching a maximum of 0.91 m AHD, showing an increase in the marsh elevation to a high-marsh environment. Into the fibrous salt-marsh peat, there was a fall in PMSE to 0.70 m AHD, which corresponds with the diversification of the assemblages to mid- to low marsh assemblages. In total, the local PMSE estimates range from 0.68 to 0.91 m AHD with an average uncertainty of ± 0.06 m (1σ).

Wapengo stratigraphy and foraminiferal assemblages

At Wapengo we established three coring transects, each from the landward to the seaward edge of the marsh (Fig. 1). The deepest core reached −1.03 m AHD and the basal unit is characterized by a silty sand (Unit 3). Overlying this unit is a silt (Unit 2). This unit is ~0.17 m in thickness and the stratigraphy is characteristic of a tidal-flat environment. Above the silt is a salt-marsh peat (Unit 1) which can be subdivided into a silty peat (Unit 1b) at the base and a fibrous salt-marsh peat at the top (Unit 1a). The area of thickest peat is noted from 0.73 to 0.97 m AHD (Fig. 3b).

The foraminiferal assemblage in the silty sand unit largely consists of *T. inflata*, *E. macrescens* and *H. wilberti* (averaging 69, 11 and 9% respectively), although total counts are low (average 26 individuals). The silt unit includes *T. inflata* and *M. fusca*; however, again, foraminiferal density is low (average of 15 individuals). *Trochamminita salsa* and *T. inflata* become dominant towards the top of the silt unit. The base of the silty peat contains *T. salsa* (average 23%, maximum 60%), although this decreases up the unit and is replaced by high counts of *T. inflata* (average 70%). Into the fibrous salt-marsh peat, the relative abundance of *M. fusca* and *P. ipohalina* increase and *T. inflata* remains abundant (averages of 33, 8 and 36% respectively).

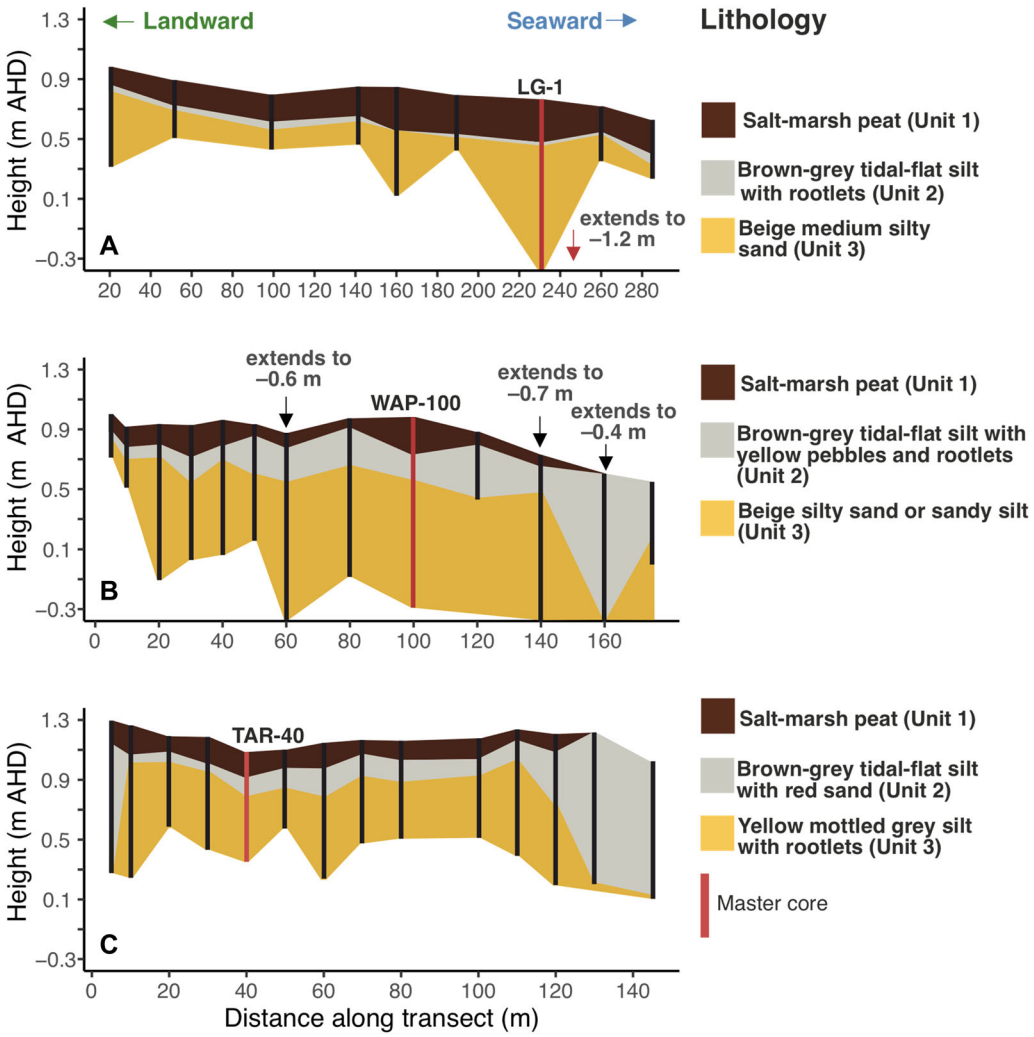

Figure 3. Stratigraphy of selected coring transects at A, Lutregala; B, Wapengo; and C, Tarra showing location of master cores used for foraminiferal and chronological analyses. [Color figure can be viewed at wileyonlinelibrary.com]

Table 2. Modern analogue technique results for each reconstruction using the local and regional transfer function models (Williams *et al.*, 2021). Samples are classified according to the 5th and 20th percentiles of their minimum dissimilarity.

Site	Model	Number of good (<5th percentile)	Number of fair (>5th percentile <20th percentile)	Number of poor (>20th percentile)
Lutregala	Regional	29	2	0
	Local	22	9	0
Wapengo	Regional	13	18	0
	Local	6	11	14
Tarra	Regional	14	13	0

Modern analogue results (Fig. 4b; Table 2) indicate that the regional training set provides a larger number of good analogues for the Wapengo core than does the local training set, as well as no poor analogues. The local model results in 14 samples with poor analogues and fewer good analogues. This is due to the moderately high relative abundance of *T. salsa* in the fossil assemblages, but low abundance in the local modern training set. *Trochamminita salsa* was often found in low count samples at Wapengo near the limit of the highest occurrence of foraminifera or highest astronomical tide, and so were not included in the training set after screening by count size (Williams et al., 2021). However, the species is more abundant in the regional training set due to the higher abundance in high total count samples at Lutregala. Williams et al. (2021) compared the modern species optima between the Wapengo local model and the regional model. As optima were consistent between models, we employ the regional transfer function.

From the sandy silt to the silt, PMSE increases by 0.19 ± 0.11 m, reaching a maximum of 0.98 m AHD, elevations associated with high-marsh environments in the modern environment. PMSE reconstructions decline from the silty peat to the fibrous peat by 0.13 ± 0.11 m to reach the core-top value of 0.81 m AHD as lower marsh foraminifera become more dominant upcore. Overall, PMSE predictions from the regional transfer function range from 0.64 to 0.98 m AHD, with an average uncertainty of ± 0.08 m (1σ).

Tarra stratigraphy and foraminiferal assemblages

At Tarra we collected cores along four transects across the marsh from the landward to the riverine edge of the marsh (Fig. 1). The deepest core extends down to –0.41 m AHD into a yellow mottled silt (Unit 3; Fig. 3c). The mottled silt is overlain by a brown–grey silt containing a small proportion of red sand (Unit 2). The brown–grey silt is overlain by a silty peat unit (Unit 1b) which is overlain by an organic salt-marsh peat

unit (Unit 1a). The area of thickest peat is found from 0.91 to 1.08 m AHD.

In the core, the yellow mottled silt unit contains very sparse foraminifera. The brown–grey silt unit largely contains *T. salsa*, *T. inflata* and *M. fusca* (average relative abundances 19, 51 and 15% respectively). Total counts of foraminifera in the unit were higher (average 163 individuals per sample). In the silty peat, *T. salsa* and *M. fusca* decreased and the relative

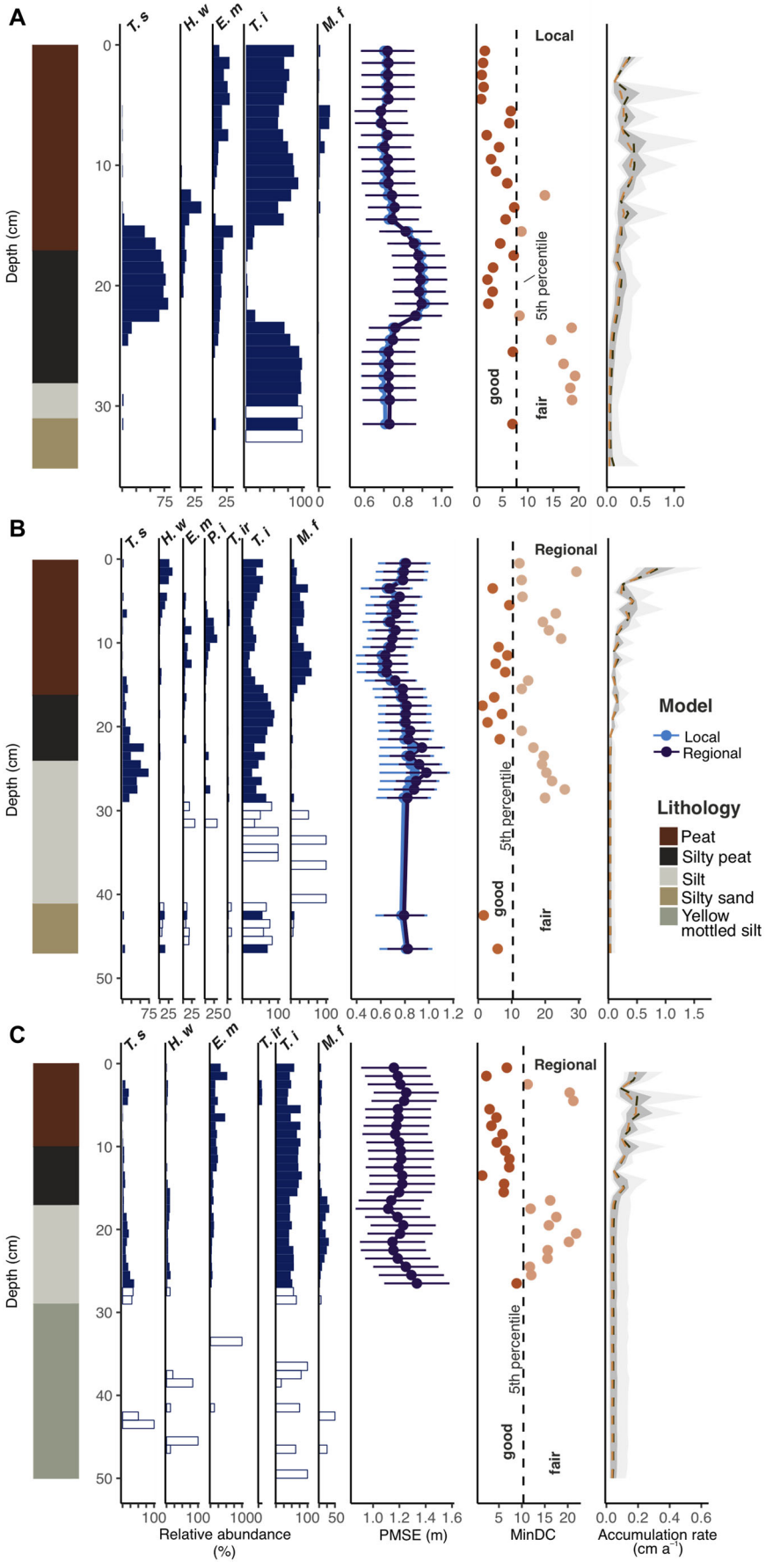

Figure 4. Core foraminifera (showing species exceeding 10% relative abundance in at least one sample), palaeomarsh surface elevation (PMSE) estimates, modern analogue results and modelled sediment accumulation rate for A, Lutregala; B, Wapengo; and C, Tarra salt marshes. Unfilled bars represent counts <50 individuals. In the accumulation rate plot, the orange dotted line = median accumulation rate, dark green dotted line = mean accumulation rate, dark grey ribbon = 68% confidence interval, light grey ribbon = 95% confidence interval. *T. s–Trochamminita salsa*, *H. w–Haplophragmoides wilberti*, *E. m –Entzia macrescens*, *P. i–Polysaccamina ipohalina*, *T. ir–Trochamminita irregularis*, *M. f–Miliammina fusca*. The accumulation rate has been derived from age–depth modelling (see 'Chronologies' section). [Color figure can be viewed at wileyonlinelibrary.com]

abundance of typical mid-marsh species *T. inflata* and *E. macrescens* increased, with *T. inflata* becoming especially dominant (average relative abundance 68%). Into the fibrous organic salt-marsh peat, assemblages remained largely similar to the silty peat, although we note an increase in the relative abundance of *E. macrescens* (average relative abundance 25%).

Modern analogue results (Fig. 4c; Table 2) show that the regional training set provides good analogues for 14 samples from the Tarra core and fair analogues for the remaining 13 samples. The majority of good analogues are found towards the top of the core where *E. macrescens* and *T. inflata* (common species in the modern training set) increase in abundance. No samples are classified as having a poor analogue, suggesting that the regional training set is representative of fossil material in the Tarra core.

PMSE could not be calculated for the yellow mottled silt unit of the core due to the low total counts. In the brown–grey silt, PMSE declined by 0.22 ± 0.18 m from 1.33 m AHD. In the peat units, PMSE remained largely uniform, showing the marsh kept pace with sea-level rise, with a small decline at the top of the core, reaching a core-top value of 1.16 m AHD. In total, PMSE predictions range from 1.12 to 1.33 m AHD with an average uncertainty of ± 0.12 m (1σ).

Chronologies

High-resolution sea-level reconstructions must be underpinned by robust and well-dated chronologies; therefore, we used a combination of radiocarbon ^{14}C AMS dating, radionuclide, stable lead ratios, as well as pollen and charcoal data to generate chronologies for each core. In the stable isotope Pb record, we identified chronohorizons including the onset of Southern Hemisphere pollution as a result of the mining, and subsequent smelting, of the Broken Hill lead–zinc–silver ore deposits (~1895 CE; Gehrels et al., 2008; Vallelonga et al., 2002). The Broken Hill smelting signal has been identified in several environmental archives across Australia (e.g. Gehrels et al., 2012; Kristensen et al., 2017; Marx et al., 2010; Wu et al., 2016). In each record, lead isotopes exhibit a distinct excursion to less radiogenic values, indicative of the lower isotopic signature of the ores compared to background (Broken hill ore: ^{206}Pb/^{207}Pb 1.04; ^{206}Pb/^{204}Pb ~16.00; ^{208}Pb/^{207}Pb 2.33; Chiaradia et al., 1997; Kristensen et al., 2017). A date of ~1890–1900 CE can be assigned to a chronohorizon where the isotopes diverge from the background rate (Gehrels et al., 2012). We also identify the Pb pollution maximum in Australia at ~1974 CE (following a peak in petrol consumption and subsequent Pb emissions; Kristensen, 2015).

At Lutregala, whilst we find exotic pollen indicative of the European settlement of Australia, other chronostratigraphic data from the core suggest that it did not appear until the mid- to late 20th century; this may be attributable to the very low population density on South Bruny Island until the late 20th century (Jackson, 2006). Similarly, no distinct horizon could be identified within the charcoal record. We obtained nine AMS ^{14}C dates from the master core (Table 3). After considering stratigraphic ordering and comparing calibrated dates to established chronohorizons, two dates were removed prior to age–depth modelling (UCIAMS-26610 and UCIAMS-236611). These dates were deemed too young for their stratigraphic position, possibly as a result of root contamination. Dates included in the model range from 1465 CE to modern. In total, we obtained 20 age estimates using this multi-dating approach and reject two (Fig. 5a; Supporting Information file 3).

Eleven samples from the Wapengo core were analysed for ^{210}Pb and we identified three chronohorizons from stable lead

Table 3. Calibrated radiocarbon dates from plant macrofossils and bulk sediment for the Lutregala, Wapengo and Tarra cores. Samples that were removed from the age–depth model prior to analysis due to their unreliable age based on their stratigraphic position are highlighted (†). Bomb-spike dates have multiple possible age ranges (see calibrated radiocarbon age column); the most likely is selected by *rplum* in age–depth modelling.

Site	Publication code	Material	Depth (cm)	Percentage modern ^{14}C (pMC) and error (1σ)	Unmodelled calibrated radiocarbon age (CE) (2σ)	δ^{13}C-VPDB (‰)
Lutregala	SUERC-93775	Grass	5	110.99 ± 0.48	1958–1959, 1994–2000	−26.9
	UCIAMS-236604	Grass	7	116.59 ± 0.19	1959–1963, 1987–1992	n.d.
	UCIAMS-236607	Grass	9	111.04 ± 0.18	1958–1959, 1995–2000	n.d.
	OZZ407	Bulk sediment	15	137.51 ± 0.35	1963, 1974–1976	−27.7 ± 0.1
	UCIAMS-236608	Grass	16	116.77 ± 0.18	1959–1963, 1987–1992	n.d.
	UCIAMS-236609	Grass	19	98.75 ± 0.18	1711–1720, 1812–1956	n.d.
	UCIAMS-236610 †	Grass	26	99.42 ± 0.18	1955–1956	n.d.
	UCIAMS-236611 †	Grass	29	100.45 ± 0.17	1955–1957	n.d.
	OZZ408	Bulk sediment	34	95.39 ± 0.23	1465, 1477–1628	−26.3 ± 0.2
Wapengo	UCIAMS-236612	Grass	3.5	108.10 ± 0.19	1958, 2000–2005	n.d.
	UCIAMS-236615	Grass	7.5	119.87 ± 0.21	1960–1963, 1985–1988	n.d.
	UCIAMS-236616	Grass	12.5	126.71 ± 0.23	1962–1963, 1980–1982	n.d.
	UCIAMS-236617 †	Grass	17.5	110.91 ± 0.19	1958–1959, 1995–2000	n.d.
	OZZ403 †	Bulk sediment	20	95.93 ± 0.28	1502–1593, 1614–1649	−26.5 ± 0.1
	UCIAMS-236618 †	Grass	24.5	108.40 ± 0.19	1956–1958, 2000–2005	n.d.
	UCIAMS-236619 †	Grass	32.5	104.03 ± 0.18	1956–1957	n.d.
	SUERC-93777	Bulk sediment	46.5	84.05 ± 0.39	638–695, 696–765	−25.9
Tarra	UCIAMS-236620	Grass	4.5	115.74 ± 0.20	1959, 1987–1993	n.d.
	SUERC-93776	Grass	6.5	125.06 ± 0.57	1962–1963, 1981–1984	−20.2
	UCIAMS-236624	Grass	11.5	130.45 ± 0.23	1963, 1978–1980	n.d.
	UCIAMS-236625 †	Grass	14.5	101.98 ± 0.18	1956–1957	n.d.
	OZZ405 †	Bulk sediment	20	93.77 ± 0.30	1411–1453	−27.1 ± 0.1
	SUERC-93778 †	Bulk sediment	24	95.85 ± 0.42	1488–1652	−25.0
	SUERC-93779 †	Bulk sediment	26	93.47 ± 0.43	1395–1453	−25.1
	OZZ406	Bulk sediment	50	84.80 ± 0.21	677–772	−26.4 ± 0.1

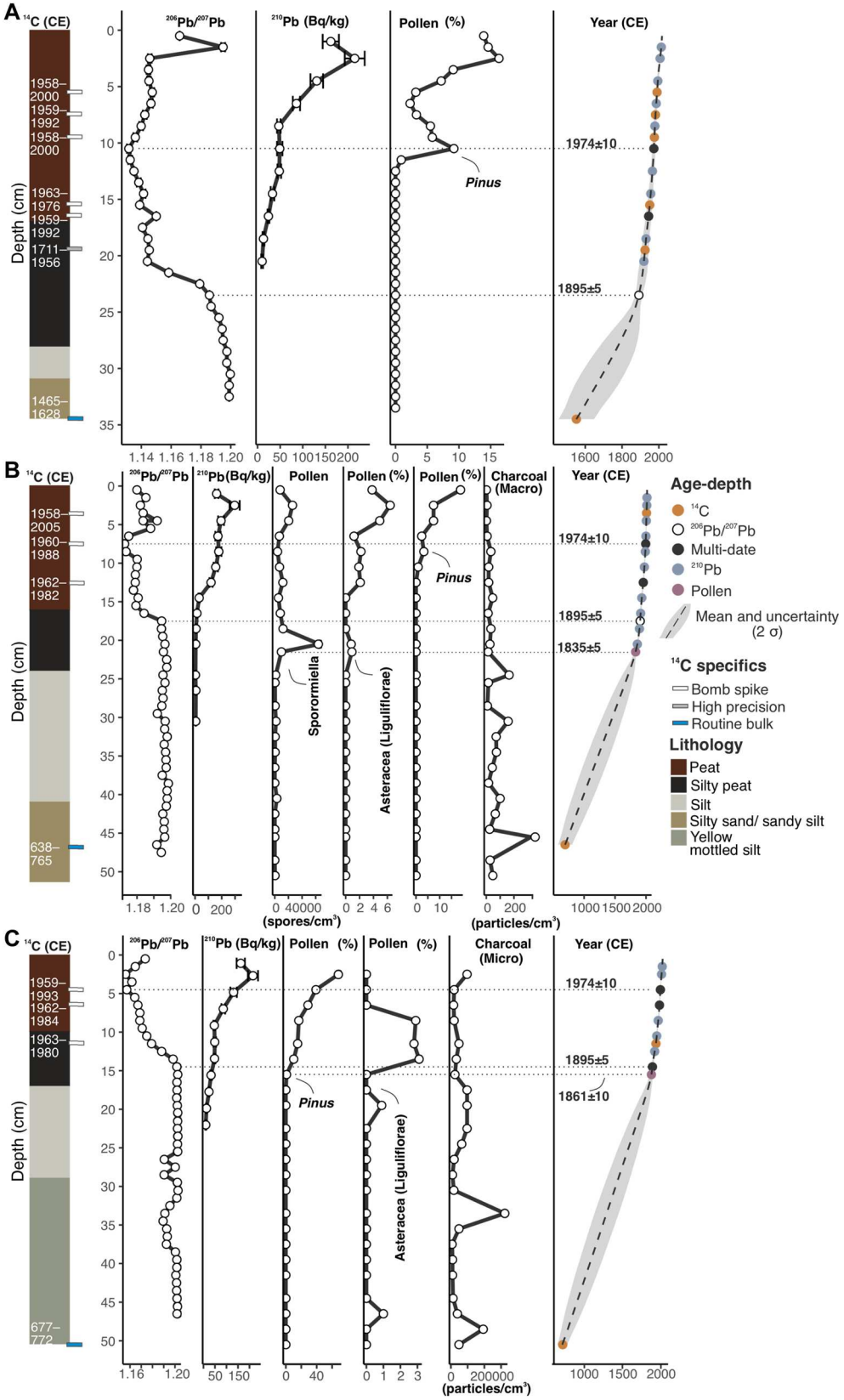

Figure 5. Core chronologies for A, Lutregala; B, Wapengo; and C, Tarra showing full 2σcalibrated ^{14}C ranges (see Table 2 for the multiple possible ranges), the identified chronohorizons from stable lead and pollen as well as the detected unsupported ^{210}Pb in the cores. The resulting age–depth model for each core is also shown – the light grey ribbon represents the 2σ age uncertainty and dotted line indicates the mean age. See Supporting Information S11–13 for full models. [Color figure can be viewed at wileyonlinelibrary.com]

isotopes and pollen (Fig. 5b). The stable isotope Pb record showed signatures of both the Broken Hill smelting as well as the Pb pollution maximum. The Pb pollution maximum was also corroborated by an increase in *Pinus* (pine) pollen at the same depth, presumably derived from pine plantations established in the 1960s–1980s (Keith & Bedward, 1999). We identified the European settlement layer from the introduction of exotic flora in the core at 21.5 cm. At the same depth, we also noted increases in *Sporormiella* (a dung fungus), which is associated with the presence of sheep and cattle in the

catchment, as pastoralism in the region began (Lunney & Leary, 1988). We obtained eight AMS ^{14}C dates from the core (Table 3). However, a visual inspection based on stratigraphic ordering, and taking into account chronohorizons from the stable lead and pollen data, suggests that samples UCIAMS-236617, UCIAMS-236618 and UCIAMS-236619 have calibrated ages that are too young for their stratigraphic position and sample OZZ403 is too old for its stratigraphic position. Sample OZZ403 was a bulk sediment sample which may have contained reworked material, and the younger dates may have been contaminated by root penetration. As clear outliers, these dates were removed from the age–depth model. Accepted ages range from 638 CE to modern. In total we accept 18 age estimations from the core and reject four (Fig. 5b; Supporting Information file 3).

Finally, eight samples were analysed for ^{210}Pb from the Tarra core and we identified three chronostratigraphic markers from stable lead isotopes and pollen (Fig. 5c) including the Broken Hill smelting, the Pb maximum and European settlement. Whilst exotic pollen taxa are noted at both 46.5 and 22.5 cm, the occurrences are isolated and do not increase significantly again until 15.5 cm. We therefore place European settlement at 15.5 cm based on the appearance and sustained increase of pine and Asteraceae (Liguliflorae, introduced European daisy) from this depth. Following Gehrels et al. (2008) we add a 20-year lag period with a ±10-year error to account for the time taken for the pine trees to produce pollen. We obtained a further eight AMS ^{14}C dates from the core (Table 3). A visual inspection using prior information from the identified chronohorizons and pollen data suggests that OZZ405, SUERC-93778 and SUERC-93779 are too old for their stratigraphic position. All three of the samples were bulk sediment and may have included reworked material. UCIAMS-236625 appears too young as it occurs at the same chronohorizon as the Broken Hill smelting and we place precedence on this marker over the ^{14}C date due to the clarity of the signal. We therefore removed these four dates from the age–depth model prior to analysis. Accepted dates range from 677 CE to modern. In total we accept 15 age estimates from the core and reject four (Fig. 5c; Supporting Information file 3).

Across all three sites, the age–depth models show low sedimentation rates in the sand and silt units at ~40–50 a cm^{-1}; however, the rates increased substantially in the salt-marsh peats to <10 a cm^{-1}. Converting these sedimentation times to accumulation rates, in the sand and silt units, accumulation was 0.02–0.03 cm a^{-1} (Fig. 4). This increased across all sites to 0.11–0.19 cm a^{-1} in the salt-marsh peats, with Tarra having a lower accumulation rate compared to Wapengo and Lutregala (Fig. 4).

In all three models, the chronology is well constrained from the mid-19th century, but age uncertainty is substantial before European settlement due to a lack of dateable organic material in the cores. Furthermore, foraminifera in the silt and silty sand units are incongruous with the facies and may reflect infaunal processes within the core. We therefore choose to base our sea-level reconstructions only on samples from the peat units where we have been able to obtain a high-resolution chronology and where foraminiferal assemblages are consistent with the sedimentary facies. This produced an RSL record from *ca.* 1830 CE to present.

Relative sea-level change in southeastern Australia

We reconstruct sea level over the last ~200 years at Lutregala, Wapengo and Tarra by combining RSL estimates with age estimations determined downcore at 1-cm resolution using the age–depth models. We also update the previously published Little Swanport reconstruction using the SHCal20 calibration curve (Hogg et al., 2020) and run the data through the same Gaussian process analysis. Corrections of −0.01 (−0.41 to 0.51; 95% confidence interval [CI]) mm a^{-1}, −0.14 (−0.52 to 0.28) mm a^{-1}, −0.25 (−1.16 to 0.30) mm a^{-1} and −0.05 (−0.70 to 0.46) mm a^{-1} was applied at Lutregala, Wapengo, Tarra and Little Swanport respectively, to account for GIA (Caron et al., 2018).

Our new reconstructions (Figs. 6 and 7) show that GIA-corrected sea level was ~0.2–0.3 m below present in the 19th century. Over the 19th century, sea-level rise was gradual at Wapengo, Tarra and Little Swanport at rates of 0.9 (−2.2 to 3.5; 95% CI) mm a^{-1} (1833–1899), 0.3 (−8.0 to 7.8) mm a^{-1} (1871–1899) and 1.0 (−2.3 to 4.3) mm a^{-1} (1822 –1899) respectively. The Lutregala record only commences in the last decade of the 19th century and longer-term trends cannot be deduced from this record.

The rate of sea-level rise increased during the first half of the 20th century (1900–1949) at all four sites to rates of 1.7 (−4.0 to 6.5; 95% CI) mm a^{-1}, 4.0 (1.2 to 7.1) mm a^{-1}, 1.4 (−2.0 to 4.7) mm a^{-1} and 4.0 (1.6 to 7.1) mm a^{-1} at Lutregala, Wapengo, Tarra and Little Swanport respectively (Fig. 7). The acceleration is especially pronounced at Wapengo and Little Swanport, although the onset of more rapid sea-level rise occurs at different times (Fig. 6). At Tarra, the reconstruction does not show evidence of a pronounced acceleration in sea level, but rather a gradual continuous rise over the 19th and 20th centuries.

Whilst maximum rates of 8.3 (4.4–16.8; 95% CI) mm a^{-1}, 5.4 (2.1–8.9) mm a^{-1} and 5.4 (3.0–8.4) mm a^{-1} are reconstructed at Lutregala, Wapengo and Little Swanport during the early to mid-20th century, maximum rates were not reached until the early 21st century at Tarra (Fig. 7). From the mid-20th century to present, the records from Lutregala, Wapengo and Little Swanport largely converge with Tarra and suggest a slowing in the rate of sea-level rise, although, due to the exceptionally high rates in the early 1950s, average rates are higher at Lutregala compared to the other sites. Our reconstructions suggest considerable regional variability with average rates of 4.6 (0.9 to 8.7) mm a^{-1}, 0.9 (−2.1 to 2.8) mm a^{-1}, 1.2 (−2.5 to 4.3) mm a^{-1} and 0.4 (−2.6 to 3.3) mm a^{-1} from 1950 to 1999 at Lutregala, Wapengo, Tarra and Little Swanport respectively.

Discussion

Synthesis of proxy and tide-gauge records

Our three new proxy records from Wapengo, Lutregala and Tarra, combined with the revised record from Little Swanport, provide a regional view of sea-level change over the last 200 years, supplementing and extending the sparse and temporally limited tide-gauge network. A comparison with tide-gauge data over the last three decades shows good agreement with our reconstructions at Lutregala and Tarra. Tide-gauge data from Stony Point, in particular, agree well with the Tarra proxy record, falling largely within the Gaussian process range. Tide-gauge data at Eden, the closest station to Wapengo, predict marginally faster rates of sea-level rise than the Gaussian process range but are within the vertical uncertainty of the data. There is little temporal overlap between available instrumental data from Spring Bay and the Little Swanport proxy record, although where the data do overlap, the observational data fall within the Gaussian process range (Fig. 6).

The oldest documented tidal measurements in Australia come from Port Arthur, Tasmania. However, the tide gauge

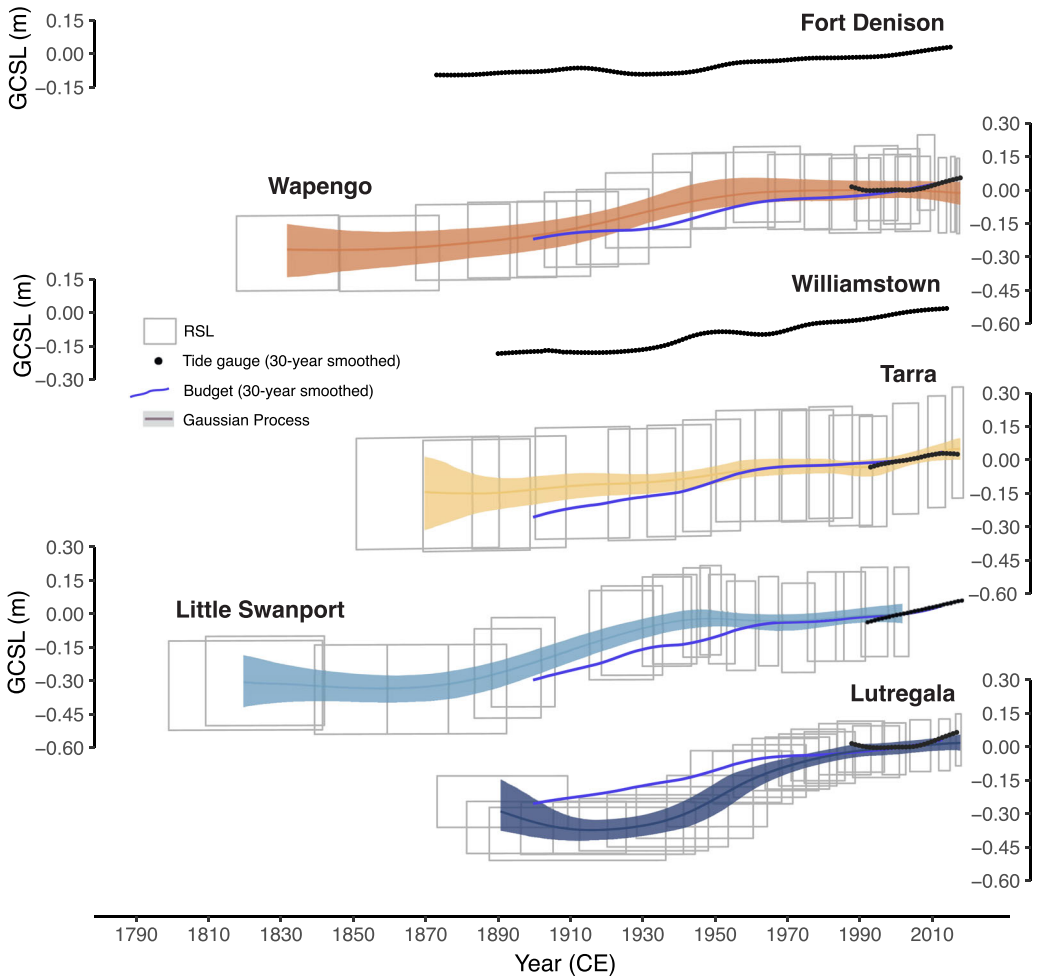

Figure 6. Comparison of GIA-corrected relative sea-level (GCSL) records from Wapengo, Tarra, Little Swanport and Lutregala showing the Gaussian process regression median and uncertainty (95% confidence intervals). Also shown are the relative sea-level estimates (grey boxes) given to 2σ. Long-term tide-gauge data (Gaussian-weighted moving average 30-year smoothed), the local modelled sea-level budget and local tide gauges (Singular Spectrum Analysis – embedding function of 15; Moore *et al.*, 2005) are also plotted. Local tide gauges for each site are: Eden (Wapengo), Stony Point (Tarra), Spring Bay (Little Swanport), Hobart (Lutregala). Sites shown trending N–S. [Color figure can be viewed at wileyonlinelibrary.com]

only recorded sea level continuously between 1841–1842 and 1999–2002 (Hunter et al., 2003). Sporadic measurements were also taken between 1875 and 1905 and in 1972. The earliest measurements from Port Arthur suggest sea level was 0.14 ± 0.04 m (2σ below present (expressed relative to 2002) in ~1841–1842 (cf. Gehrels et al., 2012). Only the Wapengo and Little Swanport records are long enough for comparison to the Port Arthur data, but the Gaussian process indicates that sea level was ~0.27 ± 0.32 and ~0.32 ± 0.45 m below present levels (2002) respectively in 1841. This indicates a discrepancy of ~0.1–0.2 m between the proxy records and the Port Arthur data for this time period. Differences cannot be related to GIA given the similarity in estimates of GIA for Tasmania and mainland Australia and the timescale of the records, but may relate to significant uncertainty surrounding the installation of the benchmark at Port Arthur (Hunter et al., 2003), or lack of high-resolution temporal data from the tide gauge. For example, some annual data in the Port Arthur record are based on a single measurement (Hunter et al., 2003). Linear regression of the tide-gauge record indicates a GIA-corrected trend of 1.0 ± 0.6 mm a^{-1} (2σ between 1841 and 2002 (Hunter et al., 2003). This is slower than both the proxy records suggest, and also slower than other long-term tide gauges from the mainland (e.g. Gehrels et al., 2012; Hogarth, 2014; White et al., 2014; Hague et al., 2021). Comparison of the trend derived from the Port Arthur tide gauge to sea-level trends from neighbouring tide gauges is not possible due to the lack of long-term data from Tasmania, and so it remains difficult to assess the veracity of the record.

When compared to the two closest near-continuous long-term tide-gauge records from the region, Fort Denison and Williamstown, only Tarra demonstrates similar magnitude rises in sea level to present (~0.20 m), with the proxy records generally suggesting larger rises in sea level than the instrumental data (~0.30–0.35 m). The few long-term tide gauges in southeastern Australia also have data gaps, subsidence issues and datum shifts, especially over the late 19th and early 20th century, which can make them problematic (e.g. Hogarth, 2014; White et al., 2014; Hague et al., 2021). Hogarth (2014) suggests that the Williamstown and Port Arthur records, in particular, should be analysed with caution. Recent efforts by Hague et al. (2021) have made corrections to the Williamstown record since 1966, and there are ongoing efforts to digitize and correct this record prior to this (B. Hague, 2022, personal communication). Similarly, in the longest record, Fort Denison, there were also issues with digitization of data, which may have led to errors in the earlier part of the record (Hamon, 1988; White et al., 2014). Hague et al. (2021) state that high-quality tide-gauge data are only available from 1966 onwards after the systematic collection of data commenced across Australia.

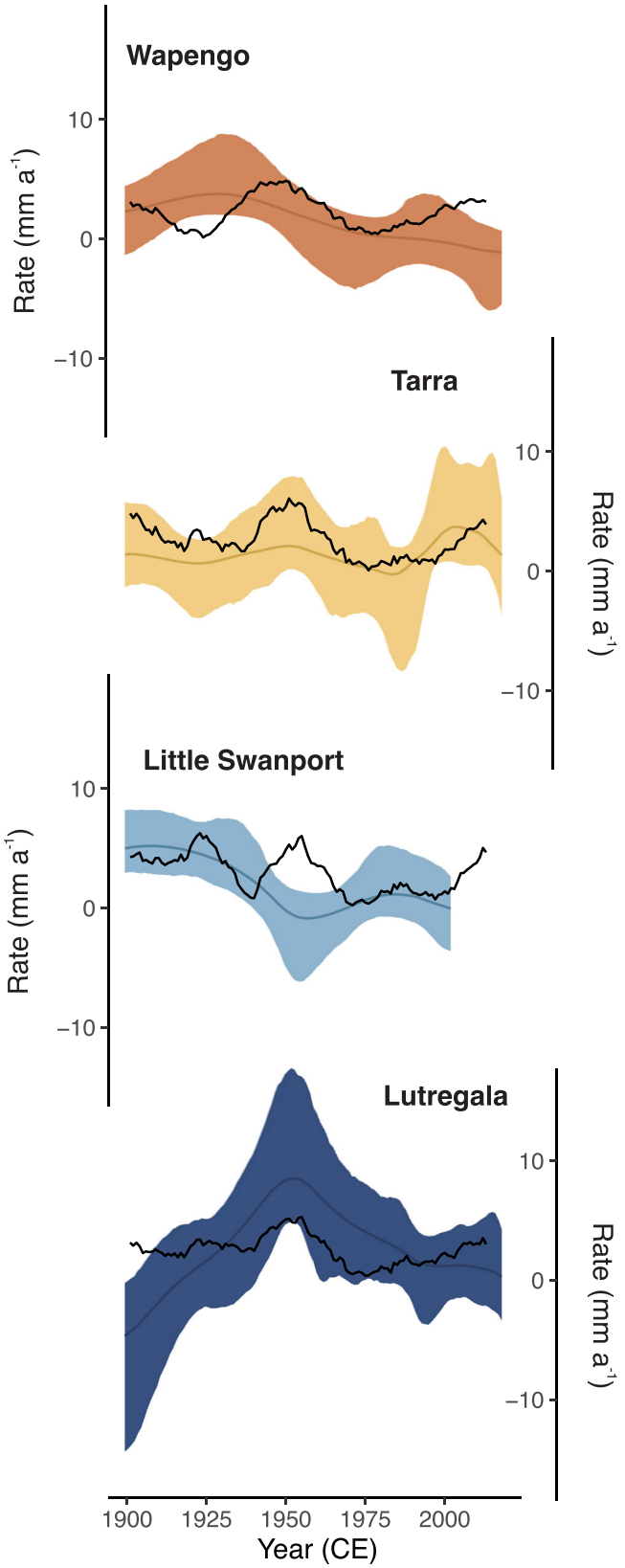

Figure 7. Comparison of the rate of relative sea-level change (95% confidence interval) at the salt marshes and the full sea-level budget (black lines, Singular Spectrum Analysis – embedding function of 15; Moore *et al.*, 2005) from 1900 to 2020. Sites shown trending N–S. [Color figure can be viewed at wileyonlinelibrary.com]

Timing of the acceleration

The ability to detect significant accelerations in sea level in instrumental records can be difficult owing to large inter-annual variations resulting from localized atmospheric and oceanic processes, as well as the necessity for records to be long enough (i.e. >40 years) to capture accelerations (e.g. Haigh et al., 2014; Steffelbauer et al., 2022). White et al. (2014) state that individual Australian tide-gauge records are too short and too variable for the detection of statistically significant accelerations in sea-level rise. Our proxy records therefore provide an alternative means for determining the timing of accelerations, albeit at a much lower temporal resolution than tide-gauge records. Average rates of sea-level change exceeded 0 mm a^{-1} in ~1833–1918 (95% CI), ~1871–2018 (95% CI), ~1821–1885 (95% CI) and ~1905–1945 (95% CI) at Wapengo, Tarra, Little Swanport and Lutregala respectively (Supporting Information Fig. S14). There is therefore significant inter-site variability in the timing of the onset of acceleration. Even when accounting for GIA uncertainty at the 95% confidence interval, there is not one common acceleration period between all of the reconstructions, suggesting other causes underlying the variability (Fig. S14).

Drivers of 20th century sea-level change

At all sites, the sum of our best estimates of sterodynamic, barystatic GRD, and inverse barometer effect contributions largely falls within the uncertainty of the reconstructions during the first half of the 20th century and generally lies within the Gaussian process ranges from ~1950 to present, suggesting that known contributors can largely explain the observed sea-level rise at our sites (Fig. 7). A discrepancy between the budget and the Wapengo reconstruction occurs between 1900 and 1925 when there is an increase in *M. fusca* in the foraminiferal population. This discrepancy may relate to infaunality of *M. fusca*, as the budget highlights a rise in sea level immediately following this increase. The largest discrepancy between the modelled budget and the proxy data is apparent in the Little Swanport reconstruction between ~1950 and 1970. This occurs where relative abundances of *T. irregularis* are highest. This resulted in high PMSE estimates in the reconstruction ~0.45–0.75 m AHD (Gehrels et al., 2012) but is contrasted by a rise in sea level in the sea-level budget. The discovery of a new foraminiferal genus and species in Australia and New Zealand *Pseudotrochamminita malcomi* (previously identified as either *T. salsa* or *T. irregularis*; King, 2021) indicates that *P. malcomi* has, overall, a lower elevation optimum than *T. salsa* and *T. irregularis*. Therefore, we suggest the PMSE estimates in this section of the core may be too high owing to the potential combining of two species into one. The discrepancy could also relate to uncertainties in the age–depth model, though we note that this section of the core is well dated by numerous chronohorizons (Gehrels et al., 2012), with the post-1975 budget aligning with the median estimates of the reconstruction.

The budget indicates that both the barystatic GRD and sterodynamic components have contributed to the rapid rates of sea-level rise. The barystatic GRD contribution was high over the first half of the 20th century. Overall, it contributed an average of 1.6 mm a^{-1} to sea level at our sites between 1900 and 1949, with greater contributions of ~2 mm a^{-1} especially between 1920 and 1940 (Fig. 8). The barystatic component also dominated early 20th century global mean sea-level rise (e.g. Parkes and Marzeion, 2018; Frederikse et al., 2020; Malles & Marzeion, 2021), with contributions primarily from land-based glaciers, as well as the Greenland and Antarctic Ice Sheets (Frederikse et al., 2020).

The sterodynamic component, as modelled in SODA, then amplified the rapid rates and subsequently drove the acceleration from ~1930 to 1940, contributing up to ~4 mm a^{-1} at its peak in the mid-20th century (Fig. 8). The increase in sterodynamic sea level may have been driven by strengthening of ocean gyres (including the East Australian Current; Cai and Cowan, 2007; Giese et al., 2016), increases in sea-surface

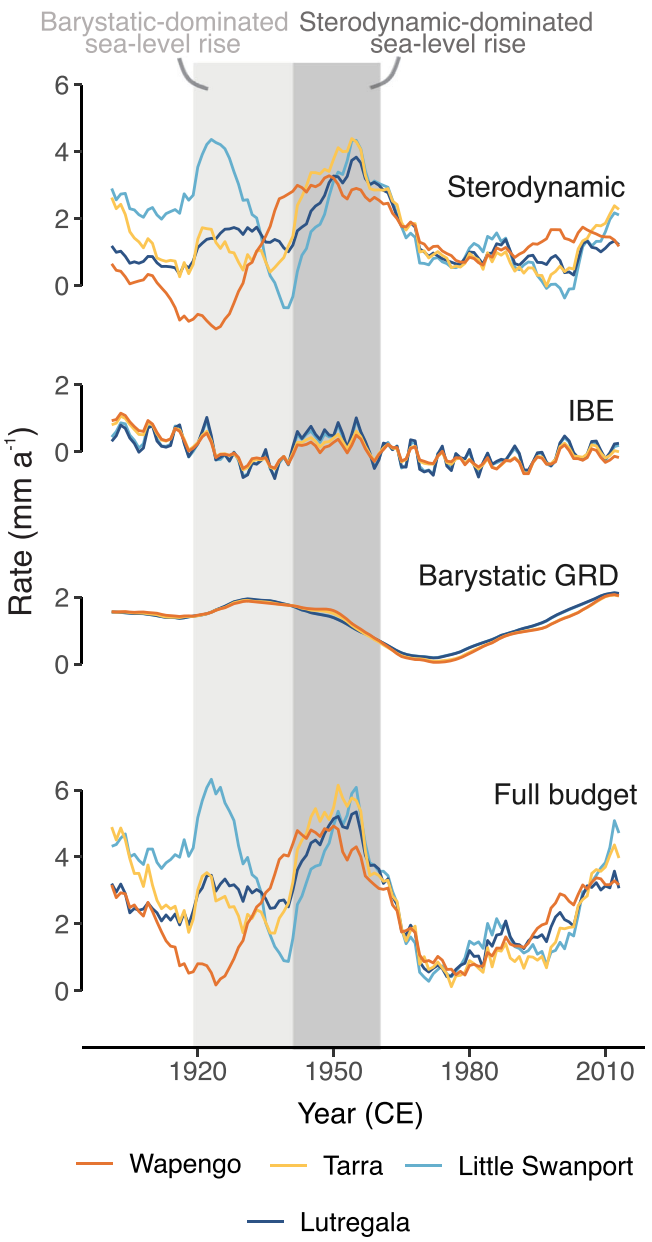

Figure 8. Contribution (mm a^{-1}) from the barystatic gravity, rotation and deformation (GRD) component, sterodynamic component and inverse barometer effect (IBE) (Singular Spectrum Analysis – embedding function of 15; Moore *et al.*, 2005) to sea level at Wapengo, Tarra, Little Swanport and Lutregala from 1900 to 2013. [Color figure can be viewed at wileyonlinelibrary.com]

temperature (especially from ~1920), changes in wind stress (Giese et al., 2016) and phase changes of several key climate modes. For example, over the early 20th century, the Interdecadal Pacific Oscillation (IPO) index declined (e.g. Salinger et al., 2001; Parker et al., 2007), changing from a positive to a negative phase change. The IPO modulates the impacts of the El Niño Southern Oscillation (ENSO) in Australia by controlling the position of the South Pacific Convergence zone and influencing sea surface temperature (and thus sea level) (e.g. Power et al., 1999; Henley et al., 2015; Kelly et al., 2019). This rapid decline in the IPO (marked by a positive increase in the rate of change of the index) is coincident with our rapid rates of sea-level rise. Additionally, an upward trend of the Southern Annular Mode (SAM) due to the depletion of ozone has resulted in higher rates of sea-level rise in the subtropical southern oceans over the late 20th century and early 21st century (Duan et al., 2021).

It is important to note that sterodynamic changes are the only component that show significant variability between the locations of our salt-marsh records. Variability is especially large over the first half of the 20th century, after which sterodynamic contributions become more comparable between sites (Fig. 8). As mentioned, this is largely replicated also in the proxy data. However, variability between modelled sterodynamic contributions may also be due to larger uncertainties in the ocean reanalysis before 1950 due to, for example, drifts resulting from less assimilated data or uncertainties in heat and freshwater fluxes (Storto et al., 2019). Even for the second half of the 20th century, ocean reanalyses often show multi-millimetre differences in linear trends of sterodynamic sea level (Dangendorf et al., 2021). Those differences become larger further back in time. Future work may seek to utilize an ensemble of sterodynamic estimates to investigate whether uncertainties in budget estimates may explain discrepancies with proxy reconstructions.

A common feature of the Lutregala, Wapengo and Little Swanport records, as well as the New Zealand proxy records (Gehrels et al., 2008; Garrett et al., 2022), is a fall or plateauing of sea level from the mid-20th century to the late 20th century. This trend has also been found in tide-gauge records around Australia and New Zealand. For example, White et al. (2014) noted a sea-level depression of ~0.2 mm a^{-1} for the majority of the east Australian coast from 1966 to 2010. Our records from Wapengo and Lutregala show a depression with average rates of ~0.0–0.1 mm a^{-1} over the same period. Similarly, Haigh et al. (2011) also observed a period of stability in tide-gauge records from Western Australia between 1950 and 1990, with a rise in the early 21st century. The stabilization in sea level in the western Pacific over the latter half of the 20th century has also been attributed to phase changes and an intensification of climate modes (e.g. Goring and Bell, 1999; Church et al., 2004; Sasaki et al., 2008; Woodworth et al., 2009; Haigh et al., 2011; Holbrook et al., 2011; Watson, 2011; White et al., 2014). An El Niño (negative ENSO) phase depressed sea level around Australia (Goring & Bell, 1999) and the index became progressively more negative after ~1960, resulting in more El Niño phases. Our (sterodynamic) budget reconstruction estimates a decline in the rate from ~1960 to 2000 coinciding with a trend of more frequent high-pressure events over Australia (Figs. 7 and 8). However, the plateau is not synchronous in time amongst the reconstructions, and therefore warrants further investigation via addition of new reconstructions in the region, and by undertaking a spatiotemporal analysis of regional sea-level trends to better decipher the regional and local non-linear and linear signals in the RSL records (cf. Walker et al., 2022).

Finally, it is possible that foraminifera respond to non-tidal (i.e. wave and wind-induced) changes in water level (Woodroffe & Long, 2010). Kemp et al. (2022) state that non-tidal water-level variability can bias reconstructions, particularly those from microtidal regimes. If non-tidal variability is relatively large in comparison to tidal variability, the relationship between elevation and inundation can be distorted. Along the US East Coast, at some sites with a tidal range <1.0 m, non-tidal forcing drove water levels above Highest Astronomical Tide. In this study, efforts have been made to accurately capture the upper limit of marine influence (i.e. inundation frequency) by using the highest occurrence of foraminifera (Wright et al., 2011; Williams et al., 2021) rather than a predicted astronomical datum. This limits bias in the accuracy and precision of the vertical uncertainty of our palaeomarsh estimates, and results in more robust reconstructions. We assume that the inundation regime has remained stationary over time, but suggest that any bias resulting from this assumption would be negligible given the centennial timescale of the study.

There is also a possibility of issues of re-working and infaunality (especially in the Little Swanport reconstruction, for which the earliest sea-level index points were derived from tidal-flat deposits). This is supported by the low accumulation rate of the tidal-flat units, low preservation of foraminifera in the units and age reversals in the chronology. Adding further high-resolution long-term records in the region will help to resolve discrepancies and further test hypotheses regarding driving mechanisms of sea-level changes in the Tasman Sea.

Conclusions

We have generated three new RSL reconstructions for southeastern Australia (Tasmania, Victoria and New South Wales) using salt-marsh foraminifera spanning the period *ca.* 1830–2018. We also updated a previously published record from Little Swanport, Tasmania (Gehrels et al., 2012), using the SHCal20 calibration curve (Hogg et al., 2020). Records from both Lutregala and Wapengo show a sea-level acceleration commencing either in the late 19th (Wapengo) or early 20th (Lutregala) century, which is consistent with the previous reconstruction from Little Swanport which exhibited an acceleration in the late 19th century, reaching maximum rates of sea-level rise in the early 20th century. The record from Tarra (Victoria), however, does not indicate a significant sea-level acceleration, but shows a gradual continuous rise in sea level to present, which is more consistent with nearby tide-gauge data. Overall, our records suggest sea level has risen by 0.2–0.3 m over the last 200 years. Similarly to previous findings from southeastern Australia and New Zealand (Gehrels et al., 2008, 2012), rates of sea-level rise in the first half of the 20th century are rapid, with average rates of up to 4.0 (−0.4 to 7.1) mm a^{-1} between 1900 and 1949.

Comparisons between tide gauge and proxy data are hindered by the lack of long-term observational data from the region. To address this issue, we compare our new records to a modelled sea-level budget for each site based on sterodynamic sea level from an ocean reanalysis model, corrected for the inverse barometer effect, and the GRD fingerprints of barystatic sea level. Comparisons between the sea-level budget and the proxy records show that the budgets are largely within the reconstruction uncertainty at all sites, and the combined sterodynamic and barystatic GRD contributions can account for the observed RSL at our sites. Future work may also seek to compare reconstructions to modelled sea-level budget estimates rather than (or alongside) tide-gauge records in regions where there is limited temporal and spatial availability of reliable tide-gauge data, such as in the Southern Hemisphere. Such work should also involve multiple ocean reanalysis products with ensemble uncertainties (Piecuch et al., 2016).

Increases in sterodynamic components (probably linked to changes in equatorial surface wind stress) have driven, in part, the rapid rates of sea-level rise in the western Pacific over the early to mid-20th century (Cai & Cowan, 2007; Giese et al., 2016). However, the rates of sea-level rise witnessed in our records are faster than those suggested from comparative sea-level records from the Northern Hemisphere (e.g. Gehrels et al., 2005; Leorri et al., 2008; Kemp et al., 2011), which raises the possibility that sea level in Australia may have been additionally driven by barystatic rise as a result of enhanced Northern Hemisphere ice melt during the early 20th century. To test this more robustly, the individual contributions from the Greenland and Antarctic Ice Sheets and land-based glaciers need to be further constrained.

Our records indicate that there is significant regional variability between the reconstructions over the first half of the 20th century, with differences in both the onset and pattern of sea-level rise. When accounting for GIA uncertainty, there is not one common acceleration period between all four reconstructions. We therefore suggest that variability may be attributed to changes in sterodynamics in the first half of the 20th century as barystatic GRD effects and inverse barometer contributions remained highly coherent between sites. However, it is possible that localized factors could be driving the variability, including foraminifera responding to wind- or wave-induced changes in water level. Adding more high-resolution proxy records and undertaking detailed spatiotemporal analyses by collating the existing and new records to isolate the local and regional non-linear signals may help elucidate sources of variability. Nonetheless, the records presented here make significant progress towards understanding early 20th century spatiotemporal patterns of RSL change in southeastern Australia. They supplement and extend the existing tide-gauge network and can be included in global analyses to address, in part, the lack of long-term sea-level data from the Southern Hemisphere.

Acknowledgements. This research was supported by the Adapting to the Challenges of a Changing Environment Doctoral Training Centre (ACCE) and funded by the Natural Environment Research Council (NERC), part of United Kingdom Research and Innovation (grant number NE/L002450/1). Funding was also provided by the Australian Nuclear and Science Technology Organisation (ANSTO). F.D.H recieved funding from the European Union's Horizon 2020 research and innovation programme under the Marie Skłodowska-Curie grant agreement (MCIRF grant number 838841—ExTaSea). Our thanks also extend to the Quaternary Research Association as well as the Menzies Centre for Australian Studies for partially funding the field campaign of this project. We would like to acknowledge the First Australians on whose lands we carried out our fieldwork. Permission to work on the land at Wapengo Marsh was granted by the New South Wales National Park and Wildlife service (licence number SL102083) as well as the landowner of Wapengo Marsh. Permission to work on Lutregala Marsh was given by the Tasmanian Land Conservancy and permission to work on Tarra Marsh was given by Parks Victoria. Thanks to Dr Katarina Jerbic (University of Bern/Flinders University), Claire Ellison, Philip Stewart (University of Queensland), Dr Matthew Meredith-Williams (La Trobe) and Nick Bowden (University of Tasmania) who provided support during the field campaign. Thanks to Kallen Marecic, Claire Ellison and Jody Daniels (all University of Queensland) for contributing to pollen analysis, and to Dr Josanne Newton (Scottish Universities Environmental Research Centre), Dr Xiaomei Xu (Keck Carbon Cycle AMS Facility) and Sabika Maizma (ANSTO) for preparing and running samples for chronological analysis. Chronological analyses were supported by ANSTO (research portal applications 12379 and 12928), the NERC Radiocarbon Facility (allocation number 2200.1019) and the NERC National Environmental Isotope Facility (IP-1938-1119). We are grateful to Dr Maarten Blaauw (Queen's University Belfast) and Dr Niamh Cahill (Maynooth University) for providing detailed insight and code for statistical modelling. Thanks also to Dr Daniel King (University of Wellington) and Ben Hague (Bureau of Meteorology/Monash University) for discussion on foraminifera and tide gauges respectively. Dr Matthew Brain (Durham University) led previous compaction experiments which were valuable to this study. Finally, we thank Dr Maria Gehrels and Mike Beckwith at the University of York and technical staff at the University of Queensland for their support.

Conflict of Interest Statement—The authors have no conflicts of interest to declare.

Data availability statement

RSL and modelled age data are available in the following Figshare repositories:

Relative sea-level data for Lutregala, Wapengo and Tarra (excel file) – https://doi.org/10.6084/m9.figshare.17129555.v1

Age data for Lutregala, Wapengo and Tarra (excel file) – https://doi.org/10.6084/m9.figshare.17129597

All other data are available in the Supporting Information of this article.

Supporting information

Additional supporting information can be found in the online version of this article.

File 1: Supporting information associated with this publication including:

S1. Preparation methodology for ^{14}C samples.

S2. Methodology for stable isotope Pb samples $^{206}Pb/^{207}Pb$.

S3. Tarra surface samples and transfer function analyses.

Fig. S3.1. Distribution of surface foraminifera at Tarra salt marsh.

Fig. S3.2. Tarra local transfer function performance.

Fig. S3.3. Species optima of the Tarra local training set and the Regional II training set.

S4. Table S4. ^{210}Pb data for core LG-1.

S5. Table S5. Stable lead isotope data for core LG-1.

S6. Table S6. ^{210}Pb data for core WAP-100.

S7. Table S7. Stable lead isotope data for core WAP-100.

S8. Table S8. ^{210}Pb data for core TAR-40.

S9. Table S9. Stable lead isotope data for core TAR-40.

S10. Table S10. Source isotope data for stable lead chronohorizon identification.

S11. Fig. S11. Age–depth model for core LG-1.

S12. Fig. S12. Age-depth model for WAP-100.

S13. Fig. S13. Age–depth model for TAR-40.

S14. Fig. S14. Sensitivity analyses of sea-level rise rate to GIA term.

Abbreviations. AMS, accelerator mass spectrometry; ACCE, Adapting to the Challenges of a Changing Environment Doctoral Training Centre; ANSTO, Australian Nuclear Science and Technology Organisation; AHD, Australian Height Datum; ENSO, El Niño Southern Oscillation; GIA, glacio-isostatic adjustment; GCSL, glacio-isostatic-adjustment-corrected sea level; GNSS, global navigation satellite system; GRD, gravity, rotation and deformation; IBE, inverse barometer effect; IPO, Interdecadal Pacific Oscillation; MCMC, Markov chain Monte Carlo; NERC, Natural Environment Research Council; PMSE, palaeomarsh surface elevation; PLS, partial least squares; RSL, relative sea level; RMSEP, root mean squared error of prediction; SAM, Southern Annular Mode; SWLI, standardized water level index; SUERC, Scottish Universities Environmental Research Centre; WAPLS, weighted averaging partial least squares; UCI, University of California, Irvine.

References

Appleby, P.G. & Oldfield, F. (1978) The calculation of lead-210 dates assuming a constant rate of supply of unsupported ^{210}Pb to the sediment. *Catena*, 5, 1–8. https://doi.org/10.1016/S0341-8162(78)80002-2

Aquino-López, M.A., Ruiz-Fernández, A.C., Blaauw, M. et al. (2020) Comparing classical and Bayesian ^{210}Pb dating models in human-impacted aquatic environments. *Quaternary Geochronology*, 60, 101106. https://doi.org/10.1016/j.quageo.2020.101106

Bamber, J. & Riva, R. (2010) The sea level fingerprint of recent ice mass fluxes. *The Cryosphere*, 4, 621–627. https://doi.org/10.5194/tc-4-621-2010

Barlow, N.L., Shennan, I., Long, A.J., Gehrels, W.R., Saher, M.H., Woodroffe, S.A. & Hillier, C. (2013) Salt marshes as late Holocene tide gauges. *Global and Planetary Change*, 106, 90–110.

Barnett, R.L., Bernatchez, P., Garneau, M. et al. (2019) Late Holocene sea-level changes in eastern Québec and potential drivers. *Quaternary Science Reviews*, 203, 151–169. https://doi.org/10.1016/j.quascirev.2018.10.039

Birks, H.J.B, Maddy, D. & Brew, J.S. (1995) Chapter 6: quantitative palaeoenvironmental reconstructions. In: Brew, JS. (Ed.) Statistical modelling of quaternary science data, Technical Guide. 5.

Blaauw, M. (2021) rplum. Available at: https://cran.r-project.org/web/packages/rplum/rplum.pdf

Brain, M.J., Long, A.J., Woodroffe, S.A. et al. (2012) Modelling the effects of sediment compaction on salt marsh reconstructions of recent sea-level rise. *Earth and Planetary Science Letters*, 345–348, 180–193. https://doi.org/10.1016/j.epsl.2012.06.045

Cai, W. & Cowan, T. (2007) Trends in Southern Hemisphere Circulation in IPCC AR4 Models over 1950–99: Ozone Depletion versus Greenhouse Forcing. *Journal of Climate*, 20, 681–693. https://doi.org/10.1175/JCLI4028.1

Caron, L., Ivins, E.R., Larour, E. et al. (2018) GIA Model Statistics for GRACE Hydrology, Cryosphere, and Ocean Science. *Geophysical Research Letters*, 45, 2203–2212. https://doi.org/10.1002/2017GL076644

Chiaradia, M., Chenhall, B.E., Depers, A.M. et al. (1997) Identification of historical lead sources in roof dusts and recent lake sediments from an industrialized area: indications from lead isotopes. *Science of the Total Environment*, 205, 107–128. https://doi.org/10.1016/S0048-9697(97)00199-X

Church, J.A. & White, N.J. (2006) A 20th century acceleration in global sea-level rise. *Geophysical Research Letters*, 33, n/a. https://doi.org/10.1029/2005GL024826

Church, J.A., White, N.J., Coleman, R. et al. (2004) Estimates of the regional distribution of sea level rise over the 1950–2000 period. *Journal of Climate*, 17, 2609–2625. https://doi.org/10.1175/1520-0442(2004)017<2609:EOTRDO>2.0.CO;2

Crawford, C. & Mitchell, I. (1999) Physical and chemical parameters of several osyter growing areas in Tasmania (Technical No. 4). Tasmanian Aquaculture & Fisheries Institute. Available at: https://eprints.utas.edu.au/6653/

Creese, R.G., Glasby, T.M., West, G. et al. (2009) *Mapping the habitats of NSW estuaries*, 113, 95. Available at. https://www.dpi.nsw.gov.au/__data/assets/pdf_file/0004/306625/AE_2009_Output-1575_Creese-et-al_Habitat-Mapping-Final-Report-113_REPORT.pdf

Dangendorf, S., Frederikse, T., Chafik, L. et al. (2021) Data-driven reconstruction reveals large-scale ocean circulation control on coastal sea level. *Nature Climate Change*, 11, 514–520. https://doi.org/10.1038/s41558-021-01046-1

Dangendorf, S., Hay, C., Calafat, F.M. et al. (2019) Persistent acceleration in global sea-level rise since the 1960s. *Nature Climate Change*, 9, 705–710. https://doi.org/10.1038/s41558-019-0531-8

Duan, J., Li, Y., Wang, F. et al. (2021) Rapid Sea-Level Rise in the Southern-Hemisphere Subtropical Oceans. *Journal of Climate*, 1, 1–55. https://doi.org/10.1175/JCLI-D-21-0248.1

Frederikse, T., Landerer, F., Caron, L., Adhikari, S., Parkes, D., Humphrey, V.W., Dangendorf, S. et al. (2020) The causes of sea-level rise since 1900. *Nature*, 584, 393–397. https://doi.org/10.1038/s41586-020-2591-3

Garrett, E., Gehrels, W.R., Hayward, B.W., Newnham, R., Gehrels, M.J., Morey, C.J. & Dangendorf, S. (2022) Drivers of 20th century sea-level change in southern New Zealand determined from proxy and instrumental records. *Journal of Quaternary Science*, 37, 1025–1043. https://doi.org/10.1002/jqs.3418

Garside, C.J., Glasby, T.M., Coleman, M.A. et al. (2014) The frequency of connection of coastal water bodies to the ocean predictsCarcinus maenasinvasion. *Limnology and Oceanography*, 59, 1288–1296. https://doi.org/10.4319/lo.2014.59.4.1288

Gehrels, W.R., Callard, S.L., Moss, P.T. et al. (2012) Nineteenth and twentieth century sea-level changes in Tasmania and New Zealand. *Earth and Planetary Science Letters*, 315–316, 94–102. https://doi.org/10.1016/J.EPSL.2011.08.046

Gehrels, W.R., Dangendorf, S., Barlow, N.L.M. et al. (2020) A Preindustrial Sea-Level Rise Hotspot Along the Atlantic Coast of North America. *Geophysical Research Letters*, 47, e2019GL085814. https://doi.org/10.1029/2019GL085814

Gehrels, W.R., Hayward, B.W., Newnham, R.M. et al. (2008) A 20th century acceleration of sea-level rise in New Zealand. *Geophysical Research Letters*, 35, L02717. https://doi.org/10.1029/2007GL032632

Gehrels, W.R., Kirby, J.R., Prokoph, A. et al. (2005) Onset of recent rapid sea-level rise in the western Atlantic Ocean. *Quaternary Science Reviews*, 24, 2083–2100. https://doi.org/10.1016/J.QUASCIREV.2004.11.016

Gehrels, W.R., Marshall, W.A., Gehrels, M.J. et al. (2006) Rapid sea-level rise in the North Atlantic Ocean since the first half of the nineteenth century. *The Holocene*, 16, 949–965. https://doi.org/10.1177/0959683606hl986rp

Gehrels, W.R. & Woodworth, P.L. (2013) When did modern rates of sea-level rise start? *Global and Planetary Change*, 100, 263–277. https://doi.org/10.1016/j.gloplacha.2012.10.020

Gerlach, M.J., Engelhart, S.E., Kemp, A.C. et al. (2017) Reconstructing Common Era relative sea-level change on the Gulf Coast of Florida. *Marine Geology*, 390, 254–269. https://doi.org/10.1016/j.margeo.2017.07.001

Giese, B.S., Seidel, H.F., Compo, G.P. et al. (2016) An ensemble of ocean reanalyses for 1815–2013 with sparse observational input. *Journal of Geophysical Research: Oceans*, 121, 6891–6910. https://doi.org/10.1002/2016JC012079

Goring, D.G. & Bell, R.G. (1999) El Niño and decadal effects on sea-level variability in northern New Zealand: A wavelet analysis. *New Zealand Journal of Marine and Freshwater Research*, 33, 587–598. https://doi.org/10.1080/00288330.1999.9516902

Hague, B.S., Jones, D.A., Trewin, B. et al. (2021) ANCHORS: A multi-decadal tide gauge dataset to monitor Australian relative sea level changes. *Geoscience Data Journal*, 9, 252–272. https://doi.org/10.1002/gdj3.136

Haigh, I.D., Eliot, M., Pattiaratchi, C. et al. (2011) Regional changes in mean sea level around Western Australia between 1897 and 2008, In: Coasts and Ports 2011: Diverse and Developing: Proceedings of the 20th Australasian Coastal and Ocean Engineering Conference and the 13th Australasian Port and Harbour Conference. Engineers Australia, 280.

Haigh, I.D., Wahl, T., Rohling, E.J. et al. (2014) Timescales for detecting a significant acceleration in sea level rise. *Nature Communications*, 5, 3635. https://doi.org/10.1038/ncomms4635

Hamon, B.V. (1988) Spurious Long-Period Tides Due to Tide Gauge Errors. The International Hydrographic Review, 65. Retrieved from: https://journals.lib.unb.ca/index.php/ihr/article/view/23384

Hay, C.C., Morrow, E., Kopp, R.E. et al. (2015) Probabilistic reanalysis of twentieth-century sea-level rise. *Nature*, 517, 481–484. https://doi.org/10.1038/nature14093

Henley, B.J., Gergis, J., Karoly, D.J. et al. (2015) A Tripole Index for the Interdecadal Pacific Oscillation. *Climate Dynamics*, 45, 3077–3090. https://doi.org/10.1007/s00382-015-2525-1

Hogarth, P. (2014) Preliminary analysis of acceleration of sea level rise through the twentieth century using extended tide gauge data sets (August 2014). *Journal of Geophysical Research: Oceans*, 119, 7645–7659. https://doi.org/10.1002/2014JC009976

Hogg, A.G., Heaton, T.J., Hua, Q. et al. (2020) SHCal20 Southern Hemisphere calibration, 0–55,000 years cal BP. *Radiocarbon*, 62, 759–778. https://doi.org/10.1017/RDC.2020.59

Holbrook, N.J., Goodwin, I.D., McGregor, S. et al. (2011) ENSO to multi-decadal time scale changes in East Australian Current transports and Fort Denison sea level: Oceanic Rossby waves as the connecting mechanism. *Deep Sea Research Part II: Topical Studies in Oceanography*, 58, 547–558. https://doi.org/10.1016/j.dsr2.2010.06.007

Hua, Q., Barbetti, M. & Rakowski, A.Z. (2013) Atmospheric radiocarbon for the period 1950–2010. *Radiocarbon*, 55, 2059–2072. https://doi.org/10.2458/azu_js_rc.v55i2.16177

Hunter, J., Coleman, R. & Pugh, D. (2003) The Sea Level at Port Arthur, Tasmania, from 1841 to the Present. *Geophysical Research Letters*, 30. https://doi.org/10.1029/2002GL016813

Jackson, R. (2006) Bruny on the Brink: Governance, Gentrification and Tourism on an Australian Island (No. 2). Available at: https://www.researchgate.net/publication/26486356_Bruny_on_the_Brink_Governance_Gentrification_and_Tourism_on_an_Australian_Island

Jevrejeva, S., Moore, J.C. & Grinsted, A. (2010) How will sea level respond to changes in natural and anthropogenic forcings by 2100? *Geophysical Research Letters*, 37. https://doi.org/10.1029/2010GL042947

Juggins, S. (2020) Package 'rioja.' Available at: https://cran.r-project.org/web/packages/rioja/rioja.pdf

Keith, D.A. & Bedward, M. (1999) Native vegetation of the South East Forests region, Eden, New South Wales. *Cunninghamia*, 6, 1–218.

Kelly, J.T., McSweeney, S., Shulmeister, J. et al. (2019) Bimodal climate control of shoreline change influenced by Interdecadal Pacific Oscillation variability along the Cooloola Sand Mass, Queensland, Australia. *Marine Geology*, 415, 105971. https://doi.org/10.1016/j.margeo.2019.105971

Kemp, A.C. & Telford, R.J. (2015) *Chapter 31:* Transfer functions. In: Shennan, I., Long, A.J., Horton & B.P. (Eds.) *Handbook of Sea-Level Research*. John Wiley & Sons. https://doi.org/10.1002/9781118452547.ch31

Kemp, A.C., Hill, T.D., Vane, C.H. et al. (2017a) Relative sea-level trends in New York City during the past 1500 years. *The Holocene*, 27, 1169–1186. https://doi.org/10.1177/0959683616683263

Kemp, A.C., Horton, B.P., Donnelly, J.P. et al. (2011) Climate related sea-level variations over the past two millennia. *Proceedings of the National Academy of Sciences*, 108, 11017–11022. https://doi.org/10.1073/pnas.1015619108

Kemp, A.C., Kegel, J.J., Culver, S.J. et al. (2017b) Extended late Holocene relative sea-level histories for North Carolina, USA. *Quaternary Science Reviews*, 160, 13–30. https://doi.org/10.1016/j.quascirev.2017.01.012

Kemp, A.C., Shaw, T.A. & Piecuch, C.G. (2022) The importance of non-tidal water-level variability for reconstructing Holocene relative sea level. *Quaternary Science Reviews*, 290, 107637. https://doi.org/10.1016/j.quascirev.2022.107637

Kemp, A.C., Sommerfield, C.K., Vane, C.H. et al. (2012) Use of lead isotopes for developing chronologies in recent salt-marsh sediments. *Quaternary Geochronology*, 12, 40–49. https://doi.org/10.1016/j.quageo.2012.05.004

Kemp, A.C., Wright, A.J. & Cahill, N. (2020) Enough is Enough, or More is More? Testing the Influence of Foraminiferal Count Size on Reconstructions of Paleo-Marsh Elevation. *Journal of Foraminiferal Research*, 50, 266–278. https://doi.org/10.2113/gsjfr.50.3.266

King, D.J. (2021) A Re-evaluation of the Foraminiferal Genus *Trochamminita* (Cushman and Brönnimann, 1948) in New Zealand and a Description of *Pseudotrochamminita Malcolmi* (New Genus, New Species). *Journal of Foraminiferal Research*, 51, 308–317. https://doi.org/10.2113/gsjfr.51.4.308

Kopp, R.E., Horton, B.P., Kemp, A.C. et al. (2015) Past and future sea-level rise along the coast of North Carolina, USA. *Climatic Change*, 132, 693–707. https://doi.org/10.1007/s10584-015-1451-x

Kopp, R.E., Kemp, A.C., Bittermann, K. et al. (2016) Temperature-driven global sea-level variability in the Common Era. *Proceedings of the National Academy of Sciences of the United States of America*, 113, 1434–41. https://doi.org/10.1073/pnas.1517056113

Kristensen, L.J. (2015) Quantification of atmospheric lead emissions from 70 years of leaded petrol consumption in Australia. *Atmospheric Environment*, 111, 195–201. https://doi.org/10.1016/j.atmosenv.2015.04.012

Kristensen, L.J., Taylor, M.P. & Flegal, A.R. (2017) An odyssey of environmental pollution: The rise, fall and remobilisation of industrial lead in Australia. *Applied Geochemistry*, 83, 3–13. https://doi.org/10.1016/J.APGEOCHEM.2017.02.007

Leorri, E., Horton, B.P. & Cearreta, A. (2008) Development of a foraminifera-based transfer function in the Basque marshes, N. Spain: implications for sea-level studies in the Bay of Biscay, *Marine Geology*, 251, 60–74. https://doi.org/10.1016/j.margeo.2008.02.005

Long, A.J., Barlow, N.L.M., Gehrels, W.R. et al. (2014) Contrasting records of sea-level change in the eastern and western North Atlantic during the last 300 years. *Earth and Planetary Science Letters*, 388, 110–122. https://doi.org/10.1016/j.epsl.2013.11.012

Long, A.J., Woodroffe, S.A., Milne, G.A., Bryant, C.L. & Wake, L.M. (2010) Relative sea level change in west Greenland during the last millennium. *Quaternary Science Reviews*, 29, 367–383. https://doi.org/10.1016/j.quascirev.2009.09.010

Lunney, D. & Leary, T. (1988) The impact on native mammals of land-use changes and exotic species in the Bega district, New South Wales, since settlement. *Austral Ecology*, 13, 67–92. https://doi.org/10.1111/j.1442-9993.1988.tb01417.x

Malles, J.-H. & Marzeion, B. (2021) Twentieth century global glacier mass change: an ensemble-based model reconstruction. *The Cryosphere*, 15, 3135–3157. https://doi.org/10.5194/tc-15-3135-2021

Marshall, W.A., Gehrels, W.R., Garnett, M.H. et al. (2007) The use of 'bomb spike' calibration and high-precision AMS ^{14}C analyses to date salt-marsh sediments deposited during the past three centuries. *Quaternary Research*, 68, 325–337. https://doi.org/10.1016/j.yqres.2007.07.005

Marx, S.K., Kamber, B.S., McGowan, H.A. et al. (2010) Atmospheric pollutants in alpine peat bogs record a detailed chronology of industrial and agricultural development on the Australian continent. *Environmental Pollution*, 158, 1615–1628. https://doi.org/10.1016/J.ENVPOL.2009.12.009

Marzeion, B., Cogley, J.G., Richter, K. et al. (2014) Attribution of global glacier mass loss to anthropogenic and natural causes. *Science*, 345, 919–921. https://doi.org/10.1126/science.1254702

Moore, J.C., Grinsted, A. & Jevrejeva, S. (2005) New tools for analyzing time series relationships and trends. *Eos, Transactions American Geophysical Union*, 86, 226–232. https://doi.org/10.1029/2005EO240003

Moss, P.T., Tibby, J., Petherick, L. et al. (2013) Late Quaternary vegetation history of North Stradbroke Island, Queensland, eastern Australia. *Quaternary Science Reviews, Linking Southern Hemisphere records and past circulation patterns: the AUS-INTIMATE project*, 74, 257–272. https://doi.org/10.1016/j.quascirev.2013.02.019

Nethery, A. (2012) Separate and Invisible A Carceral History of Australian Islands. *The International Journal of Research into Island Cultures*, 6, 85–98. Available at. https://www.shimajournal.org/issues/v6n2/i.-Nethery-Shima-v6n2-85-98.pdf

Oppenheimer, M., Glavovic, B., Hinkel, J. et al. (2019). Sea Level Rise and Implications for Low Lying Islands, Coasts and Communities.

Palmer, M.D., Domingues, C.M., Slangen, A.B.A. et al. (2021) An ensemble approach to quantify global mean sea-level rise over the 20th century from tide gauge reconstructions. *Environmental Research Letters*, 16, 044043. https://doi.org/10.1088/1748-9326/abdaec

Parker, D., Folland, C., Scaife, A. et al. (2007) Decadal to multidecadal variability and the climate change background. *Journal of Geophysical Research: Atmospheres*, 112. https://doi.org/10.1029/2007JD008411

Parkes, D. & Marzeion, B. (2018) Twentieth-century contribution to sea-level rise from uncharted glaciers. *Nature*, 563, 551–554. https://doi.org/10.1038/s41586-018-0687-9

Piecuch, C.G., Dangendorf, S., Ponte, R.M. et al. (2016) Annual Sea Level Changes on the North American Northeast Coast: Influence of Local Winds and Barotropic Motions. *Journal of Climate*, 29, 4801–4816. https://doi.org/10.1175/JCLI-D-16-0048.1

Power, S., Casey, T., Folland, C. et al. (1999) Inter-decadal modulation of the impact of ENSO on Australia. *Climate Dynamics*, 15, 319–324. https://doi.org/10.1007/s003820050284

Prahalad, V. & Jones, J. (2013) Mapping coastal saltmarshes in Southern Tasmania. Available at: https://www.nrmsouth.org.au/wp-content/uploads/2014/10/Mapping-Coastal-Saltmarshes-in-Southern-Tasmania.pdf

Saher, M.H., Gehrels, W.R., Barlow, N.L.M. et al. (2015) Sea-level changes in Iceland and the influence of the North Atlantic Oscillation during the last half millennium. *Quaternary Science Reviews*, 108, 23–36. https://doi.org/10.1016/j.quascirev.2014.11.005

Salinger, M.J., Renwick, J.A. & Mullan, A.B. (2001) Interdecadal Pacific Oscillation and South Pacific climate. *International Journal of Climatology*, 21, 1705–1721. https://doi.org/10.1002/joc.691

Sasaki, Y.N., Minobe, S., Schneider, N. et al. (2008) Decadal Sea Level Variability in the South Pacific in a Global Eddy-Resolving Ocean Model Hindcast. *Journal of Physical Oceanography*, 38, 1731–1747. https://doi.org/10.1175/2007JPO3915.1

Sim, T.G., Swindles, G.T., Morris, P.J. et al. (2021) Ecology of peatland testate amoebae in Svalbard and the development of transfer functions for reconstructing past water-table depth and pH. *Ecological Indicators*, 131, 108122. https://doi.org/10.1016/j.ecolind.2021.108122

Slangen, A.B.A., Church, J.A., Agosta, C. et al. (2016) Anthropogenic forcing dominates global mean sea-level rise since 1970. *Nature Climate Change*, 6, 701–705. https://doi.org/10.1038/nclimate2991

Slivinski, L.C., Compo, G.P., Whitaker, J.S. et al. (2019) Towards a more reliable historical reanalysis: Improvements for version 3 of the Twentieth Century Reanalysis system. *Quarterly Journal of the Royal Meteorological Society*, 145, 2876–2908. https://doi.org/10.1002/qj.3598

Steffelbauer, D.B., Riva, R.E.M., Timmermans, J.S. et al. (2022) Evidence of regional sea-level rise acceleration for the North Sea. *Environmental Research Letters*, 17, 074002. https://doi.org/10.1088/1748-9326/ac753a

Stevenson, J. & Haberle, S. (2005) Palaeoworks technical papers 5. macro charcoal analysis: a modified technique used by the department of archaeology and natural history. Department of Archaeology & Natural History, Research School of Pacific & Asian Studies, Australian National University, 8.

Storto, A., Alvera-Azcárate, A., Balmaseda, M.A. et al. (2019) Ocean Reanalyses: Recent Advances and Unsolved Challenges. *Frontiers in Marine Science*, 6, 418. https://doi.org/10.3389/fmars.2019.00418

Vallelonga, P., Van de Velde, K., Candelone, J.-P. et al. (2002) The lead pollution history of Law Dome, Antarctica, from isotopic measurements on ice cores: 1500 AD to 1989 AD. *Earth and Planetary Science Letters*, 204, 291–306. https://doi.org/10.1016/S0012-821X(02)00983-4

Walker, J.S., Kopp, R.E., Little, C.M. et al. (2022) Timing of emergence of modern rates of sea-level rise by 1863. *Nature Communications*, 13, 966. https://doi.org/10.1038/s41467-022-28564-6

Walker, J.S., Kopp, R.E., Shaw, T.A. et al. (2021) Common Era sea-level budgets along the U.S. Atlantic coast. *Nature Communications*, 12, 1841. https://doi.org/10.1038/s41467-021-22079-2

Watcham, E.P., Shennan, I. & Barlow, N.L.M. (2013) Scale considerations in using diatoms as indicators of sea-level change: lessons from Alaska. *Journal of Quaternary Science*, 28, 165–179. https://doi.org/10.1002/jqs.2592

Watson, P.J. (2011) Is there evidence yet of acceleration in mean sea level rise around mainland Australia? *Journal of Coastal Research*, 27, 368–377. https://doi.org/10.2112/JCOASTRES-D-10-00141.1

White, N.J., Haigh, I.D., Church, J.A. et al. (2014) Australian sea levels—Trends, regional variability and influencing factors. *Earth-Science Reviews*, 136, 155–174. https://doi.org/10.1016/J.EARSCIREV.2014.05.011

Williams, S., Garrett, E., Moss, P. et al. (2021) Development of a Training Set of Contemporary Salt-Marsh Foraminifera for Late Holocene Sea- Level Reconstructions in southeastern Australia. *Open Quaternary*, 7, 4. https://doi.org/10.5334/oq.93

Wold, S., Ruhe, A., Wold, H. et al. (1984) The Collinearity Problem in Linear Regression. The Partial Least Squares (PLS) Approach to Generalized Inverses. *SIAM Journal on Scientific and Statistical Computing*, 5, 735–743. https://doi.org/10.1137/0905052

Woodroffe, S.A. & Long, A.J. (2010) Reconstructing recent relative sea-level changes in West Greenland: Local diatom-based transfer functions are superior to regional models. *Quaternary International, Quaternary Land-Ocean Interactions: Driving Mechanisms and Coastal Responses*, 221, 91–103. https://doi.org/10.1016/j.quaint.2009.06.005

Woodworth, P.L., White, N.J., Jevrejeva, S. et al. (2009) Evidence for the accelerations of sea level on multi-decade and century timescales. *International Journal of Climatology*, 29, 777–789. https://doi.org/10.1002/joc.1771

Wright, A.J., Edwards, R.J. & van de Plassche, O. (2011) Reassessing transfer-function performance in sea-level reconstruction based on benthic salt-marsh foraminifera from the Atlantic coast of NE North America. *Marine Micropaleontology*, 81, 43–62. https://doi.org/10.1016/J.MARMICRO.2011.07.003

Wu, L., Taylor, M.P., Handley, H.K. et al. (2016) Australian atmospheric lead deposition reconstructed using lead concentrations and isotopic compositions of archival lichen and fungi. *Environmental Pollution*, 208, 678–687. https://doi.org/10.1016/J.ENVPOL.2015.10.046